Metal-ferroelectric supercrystals with periodically curved metallic layers

Marios Hadjimichael[1,2*†§], Yaqi Li[2*], Edoardo Zatterin[2,3], Gilbert A. Chahine[4], Michele Conroy[5], Kalani Moore[5], Eoghan N. O'Connell[5], Petr Ondrejkovič[6], Pavel Marton[6], Jiri Hlinka[6], Ursel Bangert[5], Steven Leake[3], Pavlo Zubko[1,2‡]

[1]*London Centre for Nanotechnology, 17–19 Gordon Street, London WC1H 0HA, UK.*
[2]*Department of Physics and Astronomy, University College London, Gower Street, London WC1E 6BT, UK*
[3]*ESRF, The European Synchrotron, 71 Avenue des Martyrs, Grenoble 38000, France.*
[4]*Université Grenoble Alpes, CNRS, Grenoble INP, SIMAP, 38000 Grenoble, France*
[5]*Department of Physics, Bernal Institute, University of Limerick, Ireland*
[6]*Institute of Physics of the Czech Academy of Sciences, Na Slovance 2, 18221 Praha 8, Czech Republic*

Abstract

Simultaneous manipulation of multiple boundary conditions in nanoscale heterostructures offers a versatile route to stabilising unusual structures and emergent phases. Here, we show that a stable supercrystal phase comprising a three-dimensional ordering of nanoscale domains with tailored periodicities can be engineered in $PbTiO_3$/$SrRuO_3$ ferroelectric-metal superlattices. A combination of laboratory and synchrotron X-ray diffraction, piezoresponse force microscopy, scanning transmission electron microscopy and phase-field simulations reveals a complex hierarchical domain structure that forms in order to minimize the elastic and electrostatic energy. Large local deformations of the ferroelectric lattice are accommodated by periodic lattice modulations of the metallic $SrRuO_3$ layers with curvatures up to 10^7 m^{-1}. Our results show that multidomain ferroelectric systems can be exploited as versatile templates to induce large curvatures in correlated materials, and present a route for engineering correlated materials with modulated structural and electronic properties that can be controlled using electric fields.

The rich spectrum of phenomena encountered in solid-state systems arises from the intimate coupling of the crystalline lattice with charge, orbital and spin degrees of freedom. In transition metal oxides this coupling has been extensively exploited to tune existing properties or introduce wholly new functionality through epitaxial strain engineering.[1] Among materials that are especially responsive to strain are multiaxial ferroelectrics, which naturally self-organise into ordered domain structures over a wide range of length scales.[2] Domain walls in these materials can host distinct properties of their own, acting as individual reconfigurable elements or bringing new macroscopic functionality to ultra-thin films where extremely high domain wall densities can be generated.[3] When further confined electrostatically in multilayer or superlattice geometries, strained ultrathin ferroelectrics can exhibit unusual polarisation textures, including flux closure patterns, polar vortices and arrays of chiral skyrmion bubbles that are typically forbidden in the bulk.[4-6] The response of such

* These authors contributed equally
† email: marios.hadjimichael@unige.ch (Corresponding author)
§ Present address: Department of Quantum Matter Physics, University of Geneva, Geneva, Switzerland
‡ email: p.zubko@ucl.ac.uk (Corresponding author)

systems to applied fields may lead to greatly enhanced susceptibilities and unusual behaviour as exemplified by the negative capacitance effect.[7]

Competing domain structures with similar energies can give rise to the coexistence of different polarisation textures and their facile interconversion upon electrical, mechanical or optical stimulation. A striking example is the recent observation of a metastable, optically-induced supercrystal phase observed in $PbTiO_3$/$SrTiO_3$ superlattices illuminated with above-band-gap radiation.[8] Here we show that a different supercrystal phase can be stabilized in oxide superlattices consisting of alternating layers of ferroelectric $PbTiO_3$ and a correlated metal $SrRuO_3$ without the need for optical excitation. A combined investigation of reciprocal space structure and direct-space imaging using scanning probe and transmission electron microscopies reveals a complex, hierarchical arrangement of flux closure domains and structurally modulated metallic layers with tuneable in-plane periodicity. We also show that a similar domain structure can be stabilised in hierarchical superlattices of $PbTiO_3$ and $SrTiO_3$ without conducting layers, demonstrating that this supercrystal phase arises from the combined action of epitaxial strain and poor screening of the ferroelectric polarisation. This interpretation is confirmed using phase-field simulations, which also reveal large enhancements in the dielectric response of the $PbTiO_3$ layers, associated with nanoscale domain wall motion. Finally, analysis of the structural modulations of the system shows that the ferroelectric domain structure imposes local curvatures of the order of 10^7 m^{-1} on the metallic layers, and offers a versatile template for inducing large curvatures in correlated metals.

X-ray diffraction signatures of the supercrystal phase

PTO_x/SRO_y superlattices (periodic repetitions of $PbTiO_3$/$SrRuO_3$ bilayers) with x unit cells (u.c.) of $PbTiO_3$ and y u.c. of $SrRuO_3$ per period were deposited on orthorhombic $(110)_o$ $DyScO_3$ substrates as described in Methods. The conductivity of the $SrRuO_3$ layers was determined using four-point-resistance measurements, which revealed metallic behaviour in ambient and semiconducting behaviour at low temperature (Fig S1).

The reciprocal space around the specular crystal truncation rod of a PTO_{14}/SRO_5 superlattice is shown in Fig. S2; here and henceforth, the reflections are indexed with respect to the pseudocubic perovskite unit cell. The diffraction pattern for this $PbTiO_3$/$SrRuO_3$ superlattice bears a close resemblance to that previously reported for $PbTiO_3$/$SrTiO_3$ superlattices grown on $DyScO_3$. The weakly discernible in-plane satellites, corresponding to an in-plane periodicity of 9 nm, are characteristic of regular arrays of vortex-like flux-closure domains [5,9]. Upon increasing the $PbTiO_3$ layer thickness, the modulation period increases. However, for $PbTiO_3$ layers thicker than approximately 15 u.c., the diffraction pattern changes dramatically. Synchrotron 3D reciprocal space mapping (see Fig 1 and supplementary video) reveals a striking diffraction pattern corresponding to a highly ordered 3D domain structure with an in-plane periodicity that is approximately twice that expected for the vortex phase and an out-of-plane period that is double the chemical superlattice period. For a PTO_{27}/SRO_5 superlattice with an out-of-plane (chemical) period of 12.7 nm, the in-plane domain period is approximately 26 nm. The well-defined domain satellites and finite size oscillations along the out-of-plane reciprocal space direction (Q_Z) observed in Fig 1a indicate that the domain structure is coherent across the entire superlattice thickness. The domain structure is also highly coherent along Q_X and Q_Y, with in-plane coherence lengths of the order of100 nm, while streaks of intensity along $\langle 110 \rangle_{pc}$ indicate confinement along this direction. The overall reciprocal space

picture is qualitatively similar to the optical diffraction pattern observed in $K_{1-\alpha}Li_{\alpha}Ta_{1-\beta}Nb_{\beta}O_3$ crystals with micron-scale compositional modulation,[10] and closely resembles that of the optically-induced metastable supercrystal phase recently reported in $PbTiO_3/SrTiO_3$ superlattices[8]. Our structure, however, is stable, as is demonstrated by cycling the temperature above and below the Curie point (Fig S3). On heating, the domain structure disappears above the transition temperature but reappears again on cooling, with no appreciable thermal hysteresis.

The first clues about the nature of the supercrystal phase are obtained from examining the intensity distribution of the periodic diffraction peaks. Fig 1a shows a butterfly-shaped intensity modulation reminiscent of the tilted a/c twins with alternating in-plane and out-of-plane components, which are typical of $PbTiO_3$ films on $DyScO_3$ substrates.[11] Thus, the observed 3D domain structure appears to originate from the need to minimise the elastic energy due to the lattice mismatch with the substrate. Interestingly, the scaling of lateral domain size with $PbTiO_3$ layer thickness appears to follow neither Kittel's square-root law [2,12,13] nor the linear relationship predicted by Pertsev and Zembilgotov [14,15]. Instead, we find that, for samples with $PbTiO_3$ layer thicknesses between 16 and 45 unit cells, the domain period adjusts to twice the chemical superlattice period (Fig 1d), suggesting that the structure has a tendency for maintaining the alignment of ferroelastic domain boundaries across the entire superlattice, as shown schematically in the inset of Fig 1d.

Further clues are revealed by mapping the off-specular reflections near the $\bar{1}03_{pc}$ Bragg peak of the $DyScO_3$ substrate where an unusual splitting of the domain satellite peaks is observed (Figs. 1e, 1f and S4). The superlattice Bragg peak on the crystal truncation rod exhibits a four-fold splitting, typical of in-plane twinning (so-called a_1/a_2 domains).[16] The domain structure reflections, however, show only two of the four peaks. For satellite peaks along Q_X only the peaks at lower $|Q_X|$ are present, indicating that regions of the sample with modulation along $[100]_{pc}$ have their long axis (and hence polarisation) along that direction. Conversely, only the two peaks at higher $|Q_X|$ are observed for domain structure reflections along Q_Y, indicating that the in-plane polarisation components are along $[010]_{pc}$ for regions with a modulation along $[010]_{pc}$.[16]

Piezoresponse force microscopy imaging of flux-closure domain structure

To directly image the domain structure, we perform PFM measurements on a PTO_{22}/SRO_5 superlattice where the top layer is $PbTiO_3$, rather than $SrRuO_3$. Although the electrostatic boundary conditions for this topmost $PbTiO_3$ layer are not the same as for those within the superlattice, we expect the strong elastic interactions between the layers that lead to the out-of-plane coherence of the domain structure to act equally on the topmost $PbTiO_3$ layer and force the same ferroelastic domain pattern. The results are summarised in Fig. 2a-d.

The topography of the topmost $PbTiO_3$ layer (Fig. 2a) reveals a regular nanoscale domain structure. Such topographic contrast is not expected for purely in-plane domains and indicates that both in-plane and out-of-plane domains are present. Vertical PFM (VPFM) measurements reveal regions with opposite out-of-plane polarisation arranged in a herringbone pattern with a periodicity of 22 nm along the $\langle 100 \rangle_{pc}$ and $\langle 010 \rangle_{pc}$ directions, in good agreement with XRD measurements on the same sample. The oppositely polarised domains visible in the phase image are clearly delineated by domain walls that appear as minima in the VPFM amplitude. The periodic stripes are confined within wider stripes along the $\langle 110 \rangle_{pc}$ direction, consistent with the streaky diffraction features observed in

Fig 1b and c. A similar structure is observed in the lateral PFM (LPFM) measurements, which for this cantilever orientation probes only the $[010]_{pc}$ component of polarisation. The in-plane polarised regions appear to consist of oppositely polarised stripes with head-to-head and tail-to-tail arrangements of the polarisation. To probe the perpendicular components along $[100]_{pc}$, the sample is rotated around the surface normal by 45° and 90° (Fig S5). The deduced polarisation structure is sketched next to the LPFM phase image in Fig 2b. Superposition of the LPFM and VPFM phase images reveals that domain boundaries observed in the two images are not coincident (Fig 2c). Crucially, the domain walls separating the stripes observed in VPFM appear to be offset by approximately half a domain width from those in LPFM, so that the amplitude minima in VPFM correspond to the amplitude maxima in LPFM and vice versa, as shown in Fig. 2d. These PFM signatures can be explained by a flux-closure type arrangement of ferroelectric domains sketched in Fig. 2e, which also naturally accounts for most of the features in the X-ray diffraction data. PFM switching experiments, summarised in Fig. S6, demonstrate that the flux-closure structure can be manipulated by electric fields.

Scanning transmission electron microscopy imaging

To investigate the ferroelectric domain patterns on the atomic scale and to image the stacking of the domains in the individual layers along the growth direction, we perform atomically resolved aberration corrected scanning transmission electron microscopy (STEM) measurements on different cross sections of the superlattice. The large-scale high-angle annular dark-field (HAADF) image in Fig 3a shows the full superlattice structure with well-defined layers. The $SrRuO_3$-$PbTiO_3$ interfaces are found to be asymmetric, with a higher interface roughness for the interface where $PbTiO_3$ is grown on top of $SrRuO_3$, likely due to the different growth modes of $SrRuO_3$ and $PbTiO_3$ under these conditions.[17-19] In addition to the chemical periodicity, regions of darker and lighter contrast are visible with a spacing comparable to the width of the $\langle 110 \rangle_{pc}$ stripes along $\langle 100 \rangle_{pc}$ and $\langle 010 \rangle_{pc}$, observed in PFM. The brighter regions indicate increased electron scattering consistent with the presence of multiple domain variants within the beam path, whereas the darker regions are being imaged predominantly on the zone axis. Upon magnification (Fig 3b), these darker regions reveal further contrast arising from substantial local strains that lead to a pattern indicative of flux-closure-type domains.[4] Furthermore, local strain maps obtained from geometric phase analysis (GPA)[20] and shown in Figs 3c and 3d, indicate that the $PbTiO_3$ layers consist of alternating regions with predominantly in-plane or out-of-plane polarisation. This leads to a periodic modulation of the lattice, with the $PbTiO_3$ layers bulging inwards and outwards, and the $SrRuO_3$ layers bending to accommodate this distortion as shown in Fig 3e.[21]

Combining the PFM data, cross-sectional STEM and the 3D X-ray diffraction data thus allows us to determine the complete 3D polarisation arrangement in the supercrystal phase, which takes the form of a complex hierarchical domain pattern sketched in Figs 3f and 3g.[2] We note that while our diffraction data are very similar to those reported in Ref [8], the domain pattern deduced from our measurements is very different. In particular, our proposed structure consists of 'horizontal' and 'vertical' flux-closure domains with 180° walls in the plane of the film and perpendicular to it respectively.[21] Nevertheless, despite differences in proposed structures, the observation of the supercrystal phase in metal-ferroelectric superlattices and photoexcited ferroelectric-dielectric ($PbTiO_3$/$SrTiO_3$) superlattices[8], but not in as-grown $PbTiO_3$/$SrTiO_3$ superlattices[8] poses a conundrum. On the one hand, screening by free carriers appears to be important for stabilising these

supercrystal phases. On the other hand, the appearance of flux-closure structures with no net polarisation points towards a tendency to minimize the depolarising field that usually appears in the absence of sufficient screening, and implies that it should also be possible to stabilise the supercrystal phase in non-conducting heterostructures.

Supercrystal phase in hierarchical $PbTiO_3/SrTiO_3$ superlattices

To investigate this possibility, we have deposited a hierarchical superlattice consisting of alternating blocks of $PbTiO_3$ (21 u.c. thick) separated by fine-period 1-u.c. $SrTiO_3$/1-u.c. $PbTiO_3$ superlattice spacers (5 u.c. in total), as shown schematically in Fig 4a. The 26 u.c. total period gives rise to the series of sharp superlattice reflections observed in Fig 4a. The short-period $PbTiO_3/SrTiO_3$ superlattice spacers are expected to behave effectively as a homogeneous ferroelectric with a reduced polarisation and hence create a polarisation discontinuity at the interface with the thicker $PbTiO_3$ layers. Compared to $PbTiO_3/SrRuO_3$ superlattices of the corresponding composition, reciprocal space maps for the hierarchical $PbTiO_3/SrTiO_3$ superlattice shown in Fig 4b (and S7) exhibit a more pronounced contribution from lattice tilts. However, the in-plane and out-of-plane period doubling, characteristic of the supercrystal phase, is also clearly visible. The appearance of the supercrystal phase is further confirmed by lateral PFM imaging (Fig 4c,d), which reveals regions with herringbone patterns that closely resemble those in $PbTiO_3/SrRuO_3$ superlattices in Fig 2.

The observation of a similar 3D domain structure in hierarchical $PbTiO_3/SrTiO_3$ and $PbTiO_3/SrRuO_3$ superlattices indicates that the supercrystal phase forms in response to two simultaneous constraints: the moderately tensile strain imposed by the substrate and the poor screening of the $PbTiO_3$ polarisation. This is further validated using phase-field simulations.

Phase-field simulations

To simulate the domain structure, we define a large supercell corresponding to 240 x 240 x 240 perovskite unit cells, thereby modelling 8 periods of a superlattice with 25 u.c. of $PbTiO_3$ and 5 u.c. of a dielectric spacer per period (for details, see Methods). Starting with a random polarisation distribution, the structure is relaxed over 100,000 iterations, and the resulting polarisation and strain distributions, as well as a plot of the gradient energy density, which highlights the positions of the domain walls, are shown in Fig. 5a-f. Throughout most of the simulated supercell, the polarisation distribution clearly shows a 3D ordering of vertical and horizontal flux-closure domains, closely resembling the supercrystal structure sketched in Fig 3f.

In addition to the supercrystal phase, our experiments and simulations both reveal the coexistence of another domain structure, which does not lead to the doubling of the out-of-plane superlattice period. This domain structure gives rise to an additional set of satellites in X-ray diffraction measurements (Fig S8) and corresponds to arrays of zigzagging flux-closure domains that have previously been reported in other $PbTiO_3$-based multilayers, [4,21,22] and are visible in the STEM image in Fig S9. The in-plane period corresponding to these satellites is consistent with that expected for regular arrays of flux-closure domains (including vortices) reported by other groups (Refs [5,9,23] and Fig S10). Such flux-closure patterns are also present in our phase-field simulations (see lower inset in Fig 5b and Fig S11), suggesting that this phase is close in energy to the supercrystal phase.

The stable modulated structure with controllable periodicity and a high density of domain walls observed in hierarchical $PbTiO_3/SrTiO_3$ superlattices is likely to harbour unusual elastic and dielectric properties that warrant further exploration. Our phase-field simulations, summarised in Figure S12, show that application of an electric field leads to displacements of the 180° domain walls within the vertical flux closure regions, such that *c*-domains oriented parallel to the field grow at the expense of those aligned antiparallel to it. [24] Additionally, regions with vertical flux closure grow at the expense of those occupied by horizontal flux-closure. This poling behaviour is consistent with the partial switching observed in the PFM experiments on $PbTiO_3/SrRuO_3$ superlattices in Fig. S6.

Cycling the field in our simulations leads to a slim hysteresis curve with negligible remnant polarisation (see Fig. S12), indicating that the domain wall motion is highly reversible due to the stability of the supercrystal phase. Interestingly, the highly inhomogeneous three-dimensional character of the domain structure gives rise to enhanced dielectric permittivity in all three directions. In the out-of-plane direction, the overall capacitance per unit area of the simulated structure (0.027 Fm^{-2}) is very similar to that expected from the dielectric layers alone (0.031 Fm^{-2}, with a dielectric constant of 56), indicating that the effective permittivity of the ferroelectric layers ($\sim$1800) is strongly enhanced. In addition to the enhanced out-of-plane permittivity of the $PbTiO_3$ layers, domain wall motion also leads to a similar enhancement of the in-plane response. As the dielectric and ferroelectric layers contribute in parallel along this direction, this leads to a very strong electric-field response for the supercrystal structure as a whole, with an overall in-plane dielectric constant of $\sim$1400.

The origin of the supercrystal phase

The observed three-dimensional domain structure consisting of in-plane and out-of-plane flux-closure components points to a simple mechanism for the origin of the supercrystal phase, which is summarised in Fig S13. It is known that $PbTiO_3$ films grown on a $DyScO_3$ substrate accommodate the lattice parameter mismatch by forming ferroelastic *a*/*c* domains with alternating in-plane and out-of-plane polarisation and $\{101\}_{pc}$ domain boundaries inclined at approximately 45° with respect to the substrate plane.[11] Therefore, when a $PbTiO_3/SrRuO_3$ superlattice is deposited on a $DyScO_3$ substrate, elasticity will favour this ferroelastic domain formation, with *a* and *c*-domains running through the entire thickness of the multilayer. However, in superlattice geometry, the $PbTiO_3$ film is periodically interrupted by conducting $SrRuO_3$ layers. Rather counterintuitively, these conductive layers introduce a depolarising field, as even structurally perfect $SrRuO_3/PbTiO_3$ interfaces have a finite screening length.[25] Thus, the dielectric spacers in our hierarchical $PbTiO_3/SrTiO_3$ superlattices and the imperfect screening at the interfaces in $PbTiO_3/SrRuO_3$ superlattices both lead to costly depolarising fields within the $PbTiO_3$ layers,[19] forcing the $PbTiO_3$ layers to split into vertical and horizontal flux closure domains to eliminate the macroscopic polarisation and reduce the electrostatic energy.

There are, however, a number of competing domain structures based on the a/c motif that lead to macroscopically non-polar polarisation textures. These include the regular arrays of zigzagging flux-closure domains (as in Fig S9 and Refs [4,21]), their more symmetric vortex-like analogues,[5] and the mixed a_1/a_2-vortex arrangement observed for other superlattice periodicities.[9] The supercrystal phase will therefore only appear for certain superlattice compositions, which favour the development of sufficiently strong elastic contrast between in-plane and out-of-plane distorted

regions to mediate the elastic interlayer coupling. For the vertical and horizontal flux-closure structures observed in this work, this requires the ferroelectric layer to be sufficiently thick. For thinner $PbTiO_3$ layers with finer domain periods such structures become increasingly less favourable, in part due to the increased energy cost associated with the many domain walls, and therefore other polarisation configurations may appear.[21] A different type of supercrystal phase, consisting of a simpler a/c-type pattern in the x-z plane and a vortex-like modulation along y, was instead observed in optically excited $PbTiO_3/SrTiO_3$ superlattices with thicker ($SrTiO_3$) spacer layers.[8] Here above-bandgap optical excitation was required to reduce the depolarising field and hence increase the out-of-plane distortions, which likely contribute to the necessary enhancement of the interlayer coupling. These two markedly different types of supercrystal suggest that yet other types of supercrystal ordering could be accessible by exploring superlattices with different combinations of materials, layer thicknesses, and more complex stacking sequences.[21]

Engineering periodically modulated correlated metals

One of the most striking features of the supercrystal phase is that it leads to large, periodic bending of the lattice, which creates large strain gradients within the conducting spacer layers. The corresponding curvature can be visualised in Fig. 6a, which shows a high-resolution HAADF image of the $PbTiO_3/SrRuO_3$ superlattice. The high-magnification images in Figs. 6b and 6c, and the schematic in Fig 6d show that the concave and convex distortions of the $PbTiO_3$ layer lead to large, sinusoidal-like displacements of the adjacent $SrRuO_3$ layers. Spatial mapping of the curvature in the $PbTiO_3$ and $SrRuO_3$ planes (Fig. 6e) obtained from the second derivative of the atomic displacements using the procedure described in Supplementary Materials (Fig. S14) shows that the curvature in the conducting $SrRuO_3$ layers reaches values of up to $10^7\ \mathrm{m}^{-1}$. Such large curvatures lead to strain gradients that are comparable to those found near localised defects such as dislocations, and are expected to give rise to sizeable flexoelectric effects.[26,27] As both metallicity and magnetism in $SrRuO_3$ are known to be sensitive to strain, confinement effects and interface properties,[18] the periodic bending of the $SrRuO_3$ layers in $PbTiO_3/SrRuO_3$ superlattices should also modulate their electronic and magnetic properties, which warrant further exploration. More generally, strain gradients necessarily break inversion symmetry, providing a route to engineering local polarity[28] and spin-orbit effects in metals. Metal-ferroelectric supercrystals with controllable periodicity and field-tuneable curvature thus offer a fascinating playground for manipulating the electronic structure of correlated electron materials and for exploring curvature-induced quantum phenomena.[29,30]

References

1 Schlom, D. G. *et al.* Strain tuning of ferroelectric thin films. *Annu Rev Mater Res* **37**, 589-626, doi:10.1146/annurev.matsci.37.061206.113016 (2007).

2 Roytburd, A. L., Ouyang, J. & Artemev, A. Polydomain structures in ferroelectric and ferroelastic epitaxial films. *J Phys-Condens Mat* **29**, 163001, doi:10.1088/1361-648x/29/16/163001 (2017).

3 Catalan, G., Seidel, J., Ramesh, R. & Scott, J. F. Domain wall nanoelectronics. *Rev Mod Phys* **84**, 119-156, doi:10.1103/RevModPhys.84.119 (2012).

4 Tang, Y. L. *et al.* Observation of a periodic array of flux-closure quadrants in strained ferroelectric $PbTiO_3$ films. *Science* **348**, 547-551, doi:10.1126/science.1259869 (2015).

5 Yadav, A. K. *et al.* Observation of polar vortices in oxide superlattices **530**, 198-201, (2016). *Nature* **534**, 138-138, doi:10.1038/nature17420 (2016).

6 Das, S. *et al.* Observation of room-temperature polar skyrmions. *Nature* **568**, 368-372, doi:10.1038/s41586-019-1092-8 (2019).

7 Zubko, P. *et al.* Negative capacitance in multidomain ferroelectric superlattices. *Nature* **534**, 524-528, doi:10.1038/nature17659 (2016).

8 Stoica, V. A. *et al.* Optical creation of a supercrystal with three-dimensional nanoscale periodicity. *Nat Mater* **18**, 377-383, doi:10.1038/s41563-019-0311-x (2019).

9 Damodaran, A. R. *et al.* Phase coexistence and electric-field control of toroidal order in oxide superlattices. *Nat Mater* **16**, 1003-1009, doi:10.1038/Nmat4951 (2017).

10 Pierangeli, D. *et al.* Super-crystals in composite ferroelectrics. *Nat Commun* **7**, 10674, doi:10.1038/ncomms10674 (2016).

11 Catalan, G. *et al.* Flexoelectric rotation of polarization in ferroelectric thin films. *Nat Mater* **10**, 963-967, doi:10.1038/Nmat3141 (2011).

12 Kittel, C. Theory of the Structure of Ferromagnetic Domains in Films and Small Particles. *Phys Rev* **70**, 965-971, doi:DOI 10.1103/PhysRev.70.965 (1946).

13 Schilling, A. *et al.* Scaling of domain periodicity with thickness measured in $BaTiO_3$ single crystal lamellae and comparison with other ferroics. *Phys Rev B* **74**, 024115, doi:10.1103/PhysRevB.74.024115 (2006).

14 Nesterov, O. *et al.* Thickness scaling of ferroelastic domains in $PbTiO_3$ films on $DyScO_3$. *Appl Phys Lett* **103**, 42901, doi:10.1063/1.4823536 (2013).

15 Pertsev, N. A. & Zembilgotov, A. G. Energetics and Geometry of 90-Degrees Domain-Structures in Epitaxial Ferroelectric and Ferroelastic Films. *J Appl Phys* **78**, 6170-6180, doi:Doi 10.1063/1.360561 (1995).

16 Morioka, H. *et al.* Suppressed polar distortion with enhanced Curie temperature in in-plane 90 degrees-domain structure of a-axis oriented $PbTiO_3$ Film. *Appl Phys Lett* **106**, 042905, doi:10.1063/1.4906861 (2015).

17 May, S. J. *et al.* Magnetically asymmetric interfaces in a $LaMnO_3/SrMnO_3$ superlattice due to structural asymmetries. *Phys Rev B* **77**, 174409, doi:10.1103/PhysRevB.77.174409 (2008).

18 Koster, G. *et al.* Structure, physical properties, and applications of $SrRuO_3$ thin films. *Rev Mod Phys* **84**, 253-298, doi:10.1103/RevModPhys.84.253 (2012).

19 Hadjimichael, M., Li, Y., Yedra, L., Dkhil, B. & Zubko, P. Domain structure and dielectric properties of metal-ferroelectric superlattices with asymmetric interfaces. *Physical Review Materials* **4**, 094415, doi:10.1103/PhysRevMaterials.4.094415 (2020).

20 Hytch, M. J., Snoeck, E. & Kilaas, R. Quantitative measurement of displacement and strain fields from HREM micrographs. *Ultramicroscopy* **74**, 131-146, doi:Doi 10.1016/S0304-3991(98)00035-7 (1998).

21 Liu, Y. *et al.* Large Scale Two-Dimensional Flux-Closure Domain Arrays in Oxide Multilayers and Their Controlled Growth. *Nano Lett* **17**, 7258-7266, doi:10.1021/acs.nanolett.7b02615 (2017).

22 Li, S. *et al.* Periodic arrays of flux-closure domains in ferroelectric thin films with oxide electrodes. *Appl Phys Lett* **111**, 052901, doi:10.1063/1.4996232 (2017).

23 Shafer, P. *et al.* Emergent chirality in the electric polarization texture of titanate superlattices. *P Natl Acad Sci USA* **115**, 915-920, doi:10.1073/pnas.1711652115 (2018).

24 Zubko, P., Stucki, N., Lichtensteiger, C. & Triscone, J. M. X-Ray Diffraction Studies of 180 degrees Ferroelectric Domains in $PbTiO_3/SrTiO_3$ Superlattices under an Applied Electric Field. *Phys Rev Lett* **104**, 187601, doi:10.1103/PhysRevLett.104.187601 (2010).

25 Junquera, J. & Ghosez, P. Critical thickness for ferroelectricity in perovskite ultrathin films. *Nature* **422**, 506-509, doi:10.1038/nature01501 (2003).

26 Yudin, P. V. & Tagantsev, A. K. Fundamentals of flexoelectricity in solids. *Nanotechnology* **24**, 432001, doi:10.1088/0957-4484/24/43/432001 (2013).

27 Zubko, P., Catalan, G. & Tagantsev, A. K. Flexoelectric Effect in Solids. *Annual Review of Materials Research, Vol 43* **43**, 387-421, doi:10.1146/annurev-matsci-071312-121634 (2013).
28 Kim, T. H. *et al.* Polar metals by geometric design. *Nature* **533**, 68-72, doi:10.1038/nature17628 (2016).
29 Ortix, C., Kiravittaya, S., Schmidt, O. G. & van den Brink, J. Curvature-induced geometric potential in strain-driven nanostructures. *Phys Rev B* **84**, 045438, doi:10.1103/PhysRevB.84.045438 (2011).
30 Streubel, R. *et al.* Magnetism in curved geometries. *J Phys D Appl Phys* **49**, 36, doi:10.1088/0022-3727/49/36/363001 (2016).

Correspondence and requests for materials should be addressed to M.H. (marios.hadjimichael@unige.ch) or P.Z. (p.zubko@ucl.ac.uk).

Competing interests

The authors declare no competing financial interests.

Acknowledgements

The authors would like to thank Vasiliki Tileli for preliminary TEM characterization, and ESRF for provision of synchrotron radiation facilities. Parts of this work were supported by the EPSRC through Grants EP/M007073/1 (P.Z., M.H.) and EP/S010769/1 (P.Z., Y.L., E.Z.), the China Scholarship Council (Y.L.), UCL-ESRF Impact scholarship (E.Z.) and the A. G. Leventis Foundation (M.H.). J.H. and P.O. acknowledge support from the Czech Science Foundation (project 19-28594X). M.C., K.M., E.N.O'C. and U.B. acknowledge financial support from Science Foundation Ireland (SFI 16/US/3344). M.C. acknowledges funding from SFI Industry Fellowship (18/IF/6282).

Author contributions

Sample growth and laboratory diffraction measurements were carried out by M.H. and Y.L. Synchrotron experiments were carried out by M.H., E.Z. G.A.C. and S.L., and analysed and interpreted by M.H. and P.Z. PFM measurements were carried out by Y.L. STEM sample preparation, measurements and analysis were performed by M.C., K.M., E.N.O'C. and U.B. Phase-field simulations were performed by P.O., P.M. and J.H. M.H. and P.Z. conceived the project and drafted the manuscript with input from all authors.

Methods

$PbTiO_3/SrRuO_3$ superlattices were deposited on $(110)_o$ ($(001)_{pc}$) $DyScO_3$ substrates using off-axis radiofrequency magnetron sputtering. The $PbTiO_3$ layers were deposited in a 0.18 Torr atmosphere with an oxygen:argon ratio of 20:28; the corresponding parameters for $SrRuO_3$ are 0.1 Torr and 3:60. During growth, the substrate was kept at a constant temperature of 550°C, as measured by a thermocouple inside the heating block. Several series of $PbTiO_3/SrRuO_3$ superlattices were investigated, each with a fixed $SrRuO_3$ layer thickness and varying thicknesses of $PbTiO_3$.

Structural characterization of the superlattices was conducted using a Rigaku Smartlab X-ray diffractometer with a rotating anode. Synchrotron X-ray diffraction measurements were performed at beamlines ID01[31] and BM02[32] at the European Synchrotron Radiation Facility (ESRF). Reciprocal space maps in Fig 1 and Fig S4 were obtained at beamline BM02 using a 48 µm x 94 µm, 8 keV beam and a D5 ImXpad detector. Data presented in the supplementary video was measured at beamline ID01 using a Maxipix 2D detector. Atomic force microscopy (AFM) was used to characterize the surface of the superlattices, using a Bruker Dimension Icon microscope and silicon AFM probes with a Pt/Ir conductive coating and stiffness of 0.2N/m. For domain mapping, an AC voltage with amplitude of 1V peak-to-peak near the contact resonance frequency was applied.

An electron transparent cross-section of the sample was prepared for STEM using a dual-beam focused ion beam (FIB) integrated scanning electron microscope (Thermo-Fisher Scientific FEI Helios 660 and G4 CHX models). The specimen was mounted onto an Omniprobe® copper-based lift-out grid. The sample was thinned to electron transparency in four steps: (i) from 2 µm to 800 nm using a 30 keV, 0.23 nA Ga ion beam, (ii) 800 nm to 500 nm at 16 keV, 50 pA, (iii) 500 nm to 300 nm at 8 keV, 50 pA , and (iv) <100 nm at 5 keV, 46 pA, followed by a final polishing step at 2 keV and 9 pA. The STEM analysis was performed using a Thermo-Fisher Scientific double tilt STEM holder in the Thermo-Fisher Scientific FEI double aberration-corrected monochromated Titan Themis Z at the University of Limerick. The microscope was operated at 300 kV. The imaging mode used was STEM at 146 and 230 mm camera length with a 50 µm C2 aperture. To highlight the lattice bending in Fig 3e, a fast Fourier transform (FFT) was performed on the STEM HAADF image; the out-of-plane periodicities were isolated by retaining only reciprocal space around the 00L (L≠0) spots and then performing an inverse FFT. The resulting image was then cropped and compressed horizontally to accentuate the lattice bending. GPA analysis was performed using the Strain++ open-source software available at https://jjppeters.github.io/Strainpp/. Atom position finding and 2D Gaussian refinement were completed with the Atomap Python package.[33]

Phase-field simulations were carried out using the program Ferrodo,[34,35] which solves the time-dependent Ginzburg-Landau equation for an energy potential defined by the generalized Ginzburg-Landau-Devonshire model.[36] Ferroelectric $PbTiO_3$ was described by a model compiled from literature data (model I of Ref. [36], i.e. Landau parameters at 298 K: $\alpha_1 = -1.709\times10^8$ JmC^{-2}, $\alpha_{11} = -7.25\times10^7$ Jm^5C^{-4}, $\alpha_{12} = 7.5\times10^8$ Jm^5C^{-4}, $\alpha_{111} = 2.61\times10^8$ Jm^9C^{-6}, $\alpha_{112} = 6.1\times10^8$ Jm^9C^{-6}, $\alpha_{123} = -3.66\times10^9$ Jm^9C^{-6}, gradient parameters: $G_{11} = 1\times10^{-10}$ Jm^3C^{-2}, $G_{12} = -1\times10^{-10}$ Jm^3C^{-2}, $G_{44} = 1\times10^{-10}$ Jm^3C^{-2}, elastic components: $C_{11} = 1.746\times10^{11}$ Jm^{-3}, $C_{12} = 7.94\times10^{10}$ Jm^{-3}, $C_{44} = 1.111\times10^{11}$ Jm^{-3}, electrostriction parameters: $q_{11} = 1.1412\times10^{10}$ JmC^{-2}, $q_{12} = 4.6\times10^8$ JmC^{-2}, $q_{44} = 7.5\times10^9$ JmC^{-2}, $Q_{11} = 0.089$ m^4C^{-2}, $Q_{12} = -0.026$ m^4C^{-2}, $Q_{44} = 0.0675$ m^4C^{-2}, and we used $\varepsilon_B = 1$ for the background permittivity in the expression for the dipole-dipole interaction). To simulate the effect of the nonferroelectric perovskite spacers, we have

assumed a paraelectric dielectric material with an isotropic Landau potential (α_1 = 1x10^9 JmC^{-2}, α_{11} = 1x10^9 Jm^{5}C^{-4}, α_{111} = 1x10^{10} Jm^{9}C^{-6}) but otherwise the same gradient, elastic, electrostriction and electrostatic terms as its ferroelectric counterpart. The simulations were performed on a simulation box of 240 x 240 x 240 sites consisting of 8 superlattice periods along the *z* axis, each with 25 sites of $PbTiO_3$ and 5 sites of the dielectric spacer. The spatial step was 0.4 nm. The domain structure in Fig. 5 was relaxed over 100000 iterations from a white-noise initial condition under periodic boundary conditions and epitaxial clamping conditions on the average in-plane strain (e_{xx} = 0.001, e_{yy} = 0, e_{xy}= 0). Simulations under external electric field were performed on a simulation box of 240 × 1 × 240 sites, having the same superlattice periods. The relaxed domain structure under zero electric field contained only the flux-closure patterns observed in the supercrystal phase (see Fig. S12b). To calculate the linear dielectric susceptibility, the relaxed structure was probed under small electric fields up to 500 V/m using the procedure described in detail in Ref [37].

Data availability

The STEM dataset and analysis used for calculating the curvature of the $SrRuO_3$ layers can be found at temul-toolkit.readthedocs.io/en/latest/PTO_supercrystal_hadjimichael.html. Other datasets supporting the findings of this study are available from the corresponding authors upon reasonable request.

31 Leake, S. J. *et al.* The Nanodiffraction beamline ID01/ESRF: a microscope for imaging strain and structure. *J Synchrotron Radiat* **26**, 571-584, doi:10.1107/S160057751900078x (2019).

32 Chahine, G. A. *et al.* Advanced Non-Destructive in Situ Characterization of Metals with the French Collaborating Research Group D2AM/BM02 Beamline at the European Synchrotron Radiation Facility. *Metals-Basel* **9**, 352, doi:10.3390/met9030352 (2019).

33 Nord, M., Vullum, P. E., MacLaren, I., Tybell, T. & Holmestad, R. Atomap: a new software tool for the automated analysis of atomic resolution images using two-dimensional Gaussian fitting. *Adv Struct Chem Imag* **3**, 9, doi:10.1186/s40679-017-0042-5 (2017).

34 Marton, P. & Hlinka, J. Simulation of domain patterns in $BaTiO_3$. *Phase Transit* **79**, 467-483, doi:10.1080/01411590600892351 (2006).

35 Hlinka, J. & Marton, P. Phenomenological model of a 90 degrees domain wall in $BaTiO_3$-type ferroelectrics. *Phys Rev B* **74**, 104104, doi:10.1103/PhysRevB.74.104104 (2006).

36 Ondrejkovic, P., Marton, P., Stepkova, V. & Hlinka, J. Fundamental properties of ferroelectric domain walls from Ginzburg-Landau models In: *Domain Walls: from fundamental properties to nanotechnology. Edited by: Dennis Meier, Jan Seidel, Marty Gregg, Ramamoorthy Ramesh, Oxford University Press (2020). © Oxford University Press. DOI: 10.1093/oso/9780198862499.003.0006* (in press).

37 Everhardt, A. S. *et al.* Temperature-independent giant dielectric response in transitional $BaTiO_3$ thin films. *Appl Phys Rev* **7**, 011402, doi:10.1063/1.5122954 (2020).

Figure captions

Figure 1 | Reciprocal space view of the three-dimensional domain structure. a. Synchrotron X-ray diffraction reciprocal space map in the Q_X-Q_Z plane around the 002_{pc} (220_o) substrate reflection for a PTO_{27}/SRO_5 superlattice showing the periodic satellite peaks arising from a highly ordered domain lattice with long-range coherence along the $[001]_{pc}$ direction. b-c. 2D cuts through reciprocal space in the $Q_Z = 3.042$ Å^{-1} and $Q_Z = 3.017$ Å^{-1} planes (indicated by the solid red and dashed blue arrows in panel a respectively) detailing the arrangement of in-plane and out-of-plane ordering, the long-range coherence of the domains along $<100>_{pc}$ and the streaky diffuse scatter along $<110>_{pc}$. The vertical streaks of low intensity near $Q_X = 0$ in b and c are due to the filters used to attenuate the incident beam close to the substrate Bragg peak. d. The in-plane periodicity of the domain superlattice is equal to twice the chemical out-of-plane superlattice period. e. In-plane reciprocal space around the $\overline{1}03_{pc}$ substrate reflection revealing splitting of the superlattice peaks due to in-plane twinning. f. Schematic highlighting the in-plane domain variants responsible for each reflection in e.

Figure 2|Piezoresponse force microscopy (PFM) characterization of flux closure domains. a. Topography scan, showing minima and maxima associated with an alternating in-plane and out-of-plane domain structure. b. Vertical PFM (VPFM) and lateral PFM (LPFM) amplitude (in arbitrary units) and phase, showing periodic arrays of up-down domains, and head-to-head and tail-to-tail in-plane components. c. Overlay of LPFM and VPFM phase images. d. Phase profiles along the dashed line in panel c, showing that the VPFM and LPFM phases are offset by approximately a quarter of the domain period. The bottom schematic is a sketch of the domain structure compatible with the PFM data.

Figure 3|Electron microscopy characterisation of the supercrystal phase. a. Cross-sectional STEM HAADF image of the PTO_{27}/SRO_5 superlattice, showing the full superlattice structure with well-defined periodicity. b. Higher magnification image revealing a complex, periodic arrangement of horizontal and vertical flux-closure domains. c. Out-of-plane strain (ε_{zz}) with respect to the substrate ($DyScO_3$, c = 3.946 Å) extracted using geometric phase analysis (GPA). d. In-plane strain (ε_{xx}) extracted using GPA. e. Laterally compressed HAADF image, which has been Fourier filtered to retain only the out-of-plane periodicity (as described in Methods). White curves superposed over atomic planes near the $PbTiO_3/SrRuO_3$ interfaces are included as guides to the eye to highlight the large bending of the lattice. $PbTiO_3$ layers are found to exhibit periodic expansion and contraction along the out-of-plane direction with opposite deformation in neighbouring $PbTiO_3$ layers, while the $SrRuO_3$ layers bend to accommodate this distortion. f. A 2D sketch of the domain pattern deduced from the TEM measurements. (The absolute directions of the polarisation may be reversed in the experimental image.) g. 3D sketch of the overall domain pattern deduced from XRD, PFM and TEM studies.

Figure 4| Supercrystal structure in $PbTiO_3/SrTiO_3$ hierarchical superlattices a. Specular crystal truncation rod around the 001_{pc} reflection of the $DyScO_3$ substrate demonstrating the structural periodicity along the growth direction; the sketch shows 4 periods of the hierarchical superlattice structure. b. Reciprocal space map in the Q_X-Q_Z plane around the 002_{pc} reflection of the $DyScO_3$ substrate. The intensity distribution is dominated by lattice tilts of the *a* and *c* domains and modulated by the 3D domain structure with a period of 21 nm (approximate Q_X and Q_Z positions of intensity maxima due to the supercrystal structure are indicated by vertical lines and horizontal arrows respectively, with solid arrows also indicating the positions of structural superlattice peaks). c and d. Lateral PFM amplitude and phase of images showing regions corresponding to highly ordered flux-closure domains.

Figure 5| Phase-field simulations. a. Simulated 3D spatial distribution of polarisation. The pattern appeared naturally from random white noise in a periodic supercell consisting of 8 superlattice periods each with 25 u.c. of $PbTiO_3$ and 5 u.c. of a dielectric spacer when phase-field relaxation was conducted using the Landau-Ginzburg model described in the text and Methods. Nanodomains are coloured according to the largest Cartesian component of the local polarisation. b. Enlarged areas marked on the –x and –y sides of the simulated supercell in panel *a* reveal the typical vertical and horizontal flux closure patterns (top panel) and zigzag pattern (bottom panel), similar to those observed experimentally. c. Distribution of polarisation gradient energy within the simulation supercell highlights positions of domain walls and strongly resembles the texture observed by STEM (Fig. 3b). d.-f. Strain tensor components e_{xx}, e_{yy} and e_{zz} indicate a strong correlation of the strain texture across the adjacent superlattice layers.

Figure 6| Mapping the curvature of periodically modulated $SrRuO_3$ layers. a. High-resolution HAADF image showing the coupling of structural distortions through the $SrRuO_3$ layers. b and c. Magnification of two regions near $SrRuO_3$-$PbTiO_3$ interfaces showing the vertical displacements imposed by $PbTiO_3$ on the $SrRuO_3$ lattice. d. Schematic of the structural distortions in the $PbTiO_3/SrRuO_3$ superlattice. e. Local curvature in each atomic plane. Green points mark the positions of Ti and Ru atoms, with overlaid colour map showing the magnitude and sign of the curvature imposed on the periodically modulated structure.

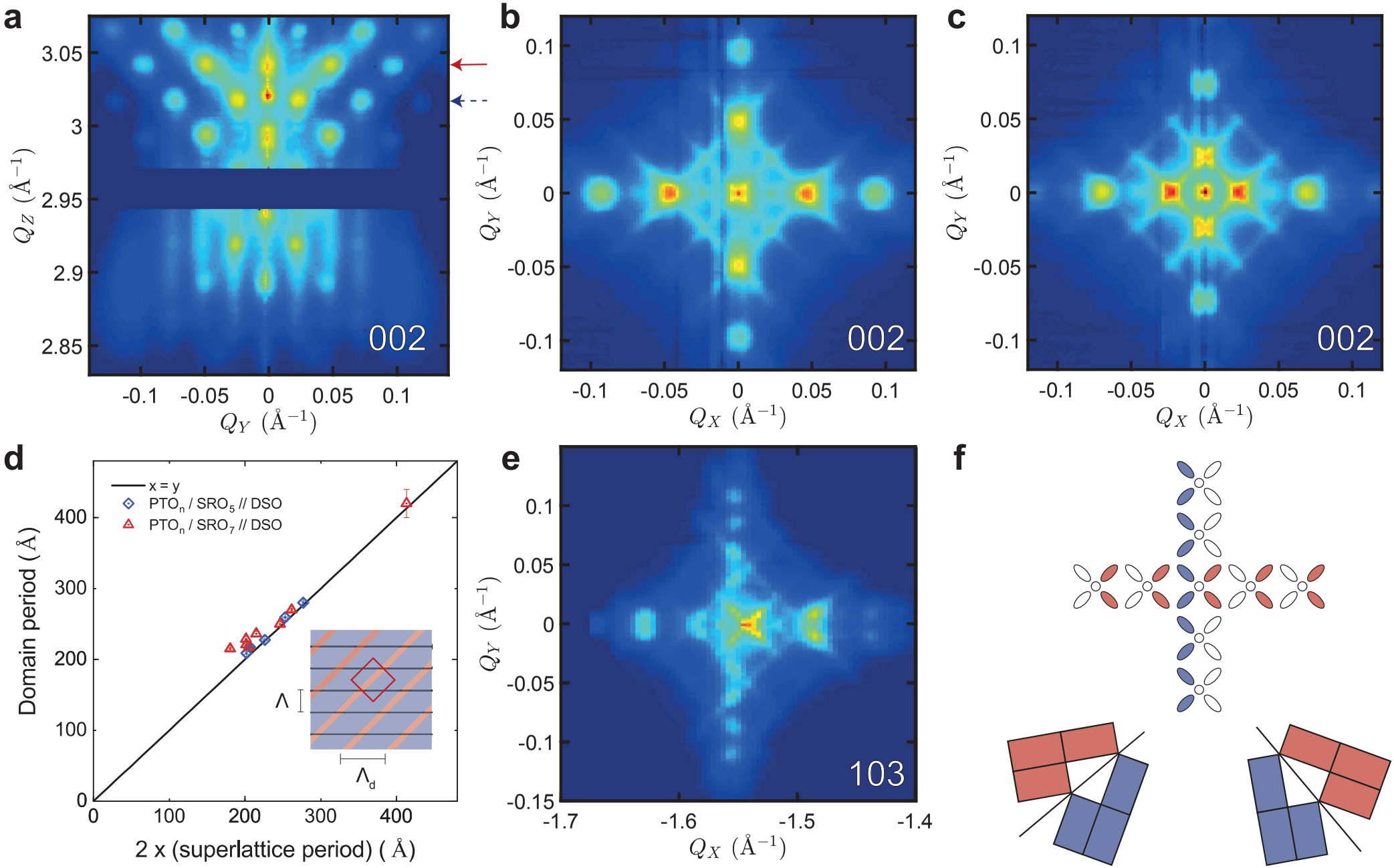
a
3.05
3
2.95
2.9
2.85
Q_Z (Å^{-1})
-0.1 -0.05 0 0.05 0.1
Q_Y (Å^{-1})
002
b
0.1
0.05
0
-0.05
-0.1
Q_Y (Å^{-1})
-0.1 -0.05 0 0.05 0.1
Q_X (Å^{-1})
002
c
0.1
0.05
0
-0.05
-0.1
Q_Y (Å^{-1})
-0.1 -0.05 0 0.05 0.1
Q_X (Å^{-1})
002
d
x = y
PTO$_n$ / SRO$_5$ // DSO
PTO$_n$ / SRO$_7$ // DSO
Domain period (Å)
0 100 200 300 400
2 x (superlattice period) (Å)
Λ
Λ$_d$
e
0.1
0.05
0
-0.05
-0.1
-0.15
Q_Y (Å^{-1})
-1.7 -1.6 -1.5 -1.4
Q_X (Å^{-1})
103
f

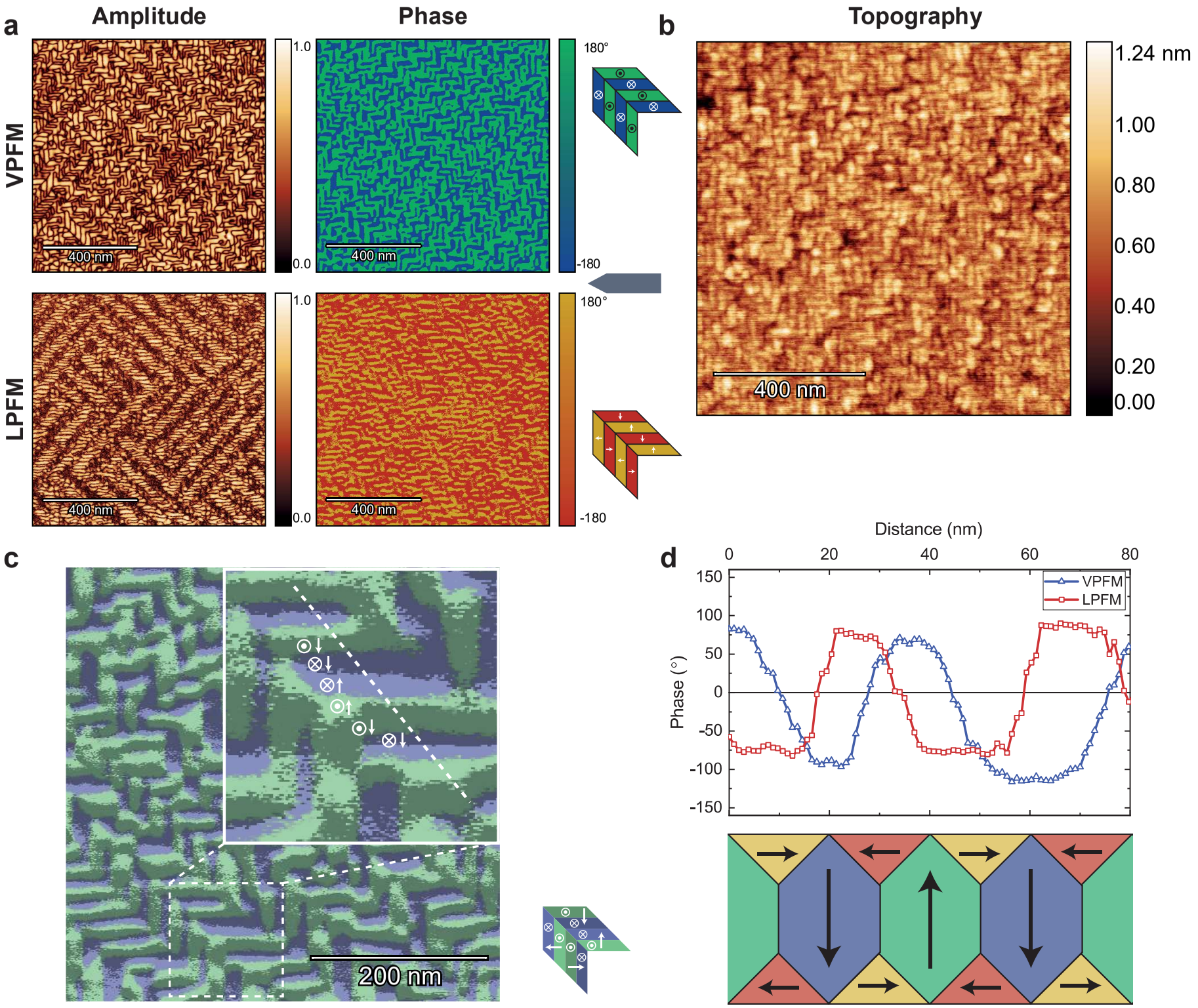
a
Amplitude
Phase
VPFM
LPFM
1.0
0.0
180°
-180
400 nm
b
Topography
1.24 nm
1.00
0.80
0.60
0.40
0.20
0.00
c
200 nm
d
Distance (nm)
0
20
40
60
80
150
100
50
0
-50
-100
-150
Phase (°)
VPFM
LPFM

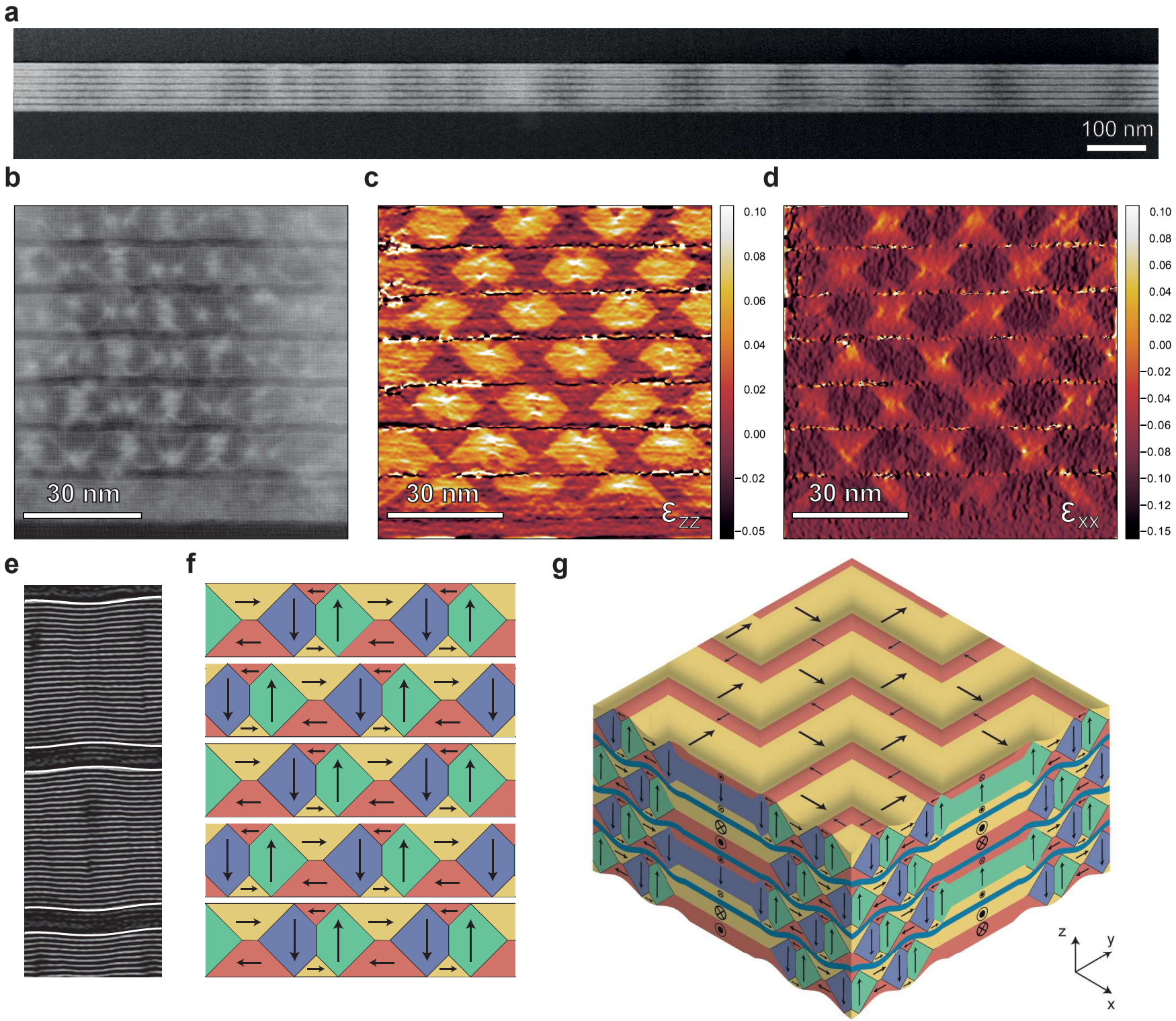
a
100 nm
b
30 nm
c
30 nm
ε_{zz}
0.10
0.08
0.06
0.04
0.02
0.00
−0.02
−0.05
d
30 nm
ε_{xx}
0.10
0.08
0.06
0.04
0.02
0.00
−0.02
−0.04
−0.06
−0.08
−0.10
−0.12
−0.15
e
f
g
z
y
x

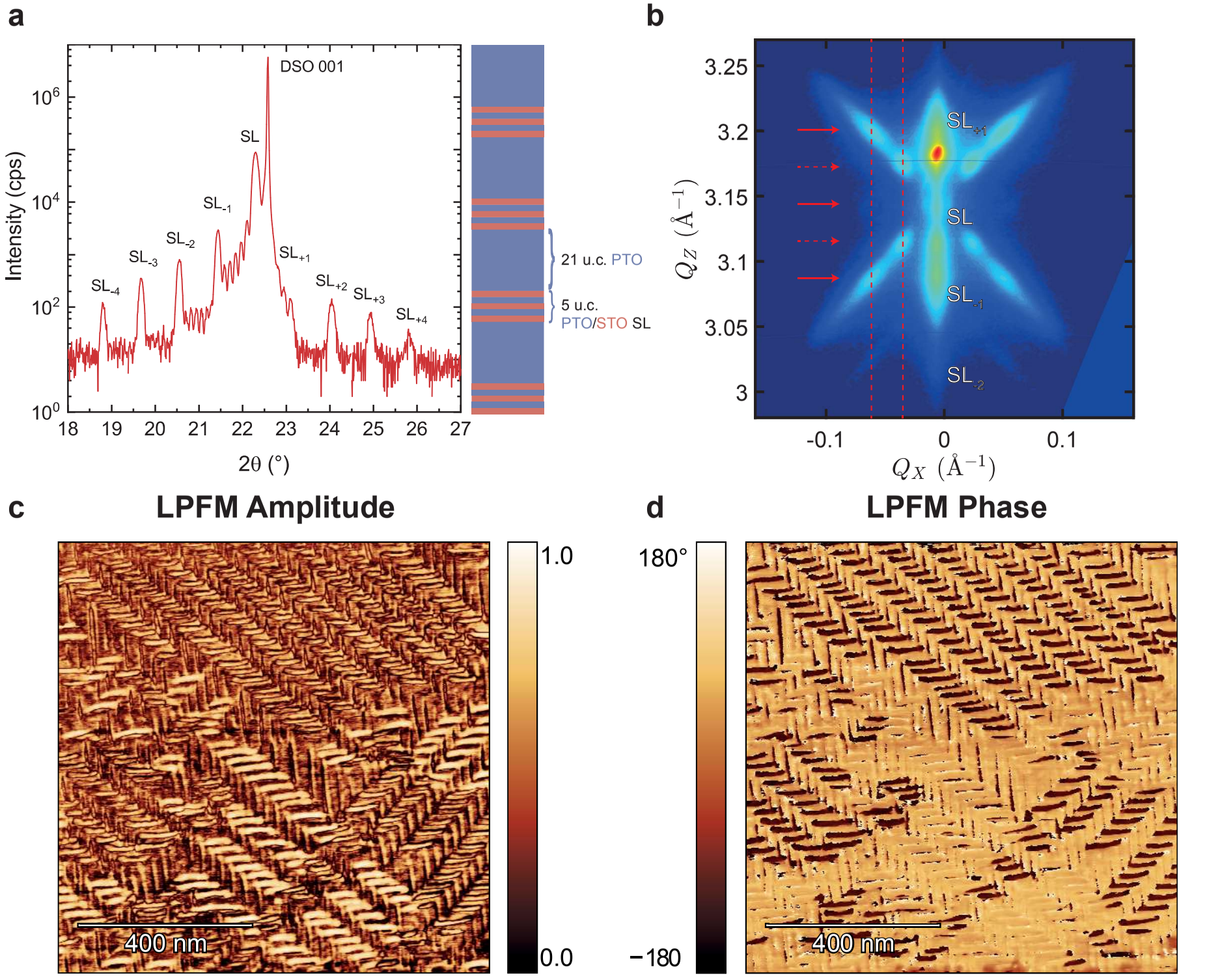
a
DSO 001
SL
SL-1
SL-2
SL-3
SL-4
SL+1
SL+2
SL+3
SL+4
Intensity (cps)
2θ (°)
21 u.c. PTO
5 u.c.
PTO/STO SL
b
SL+1
SL
SL-1
SL-2
QZ (Å−1)
QX (Å−1)
c
LPFM Amplitude
400 nm
1.0
0.0
d
LPFM Phase
180°
−180
400 nm

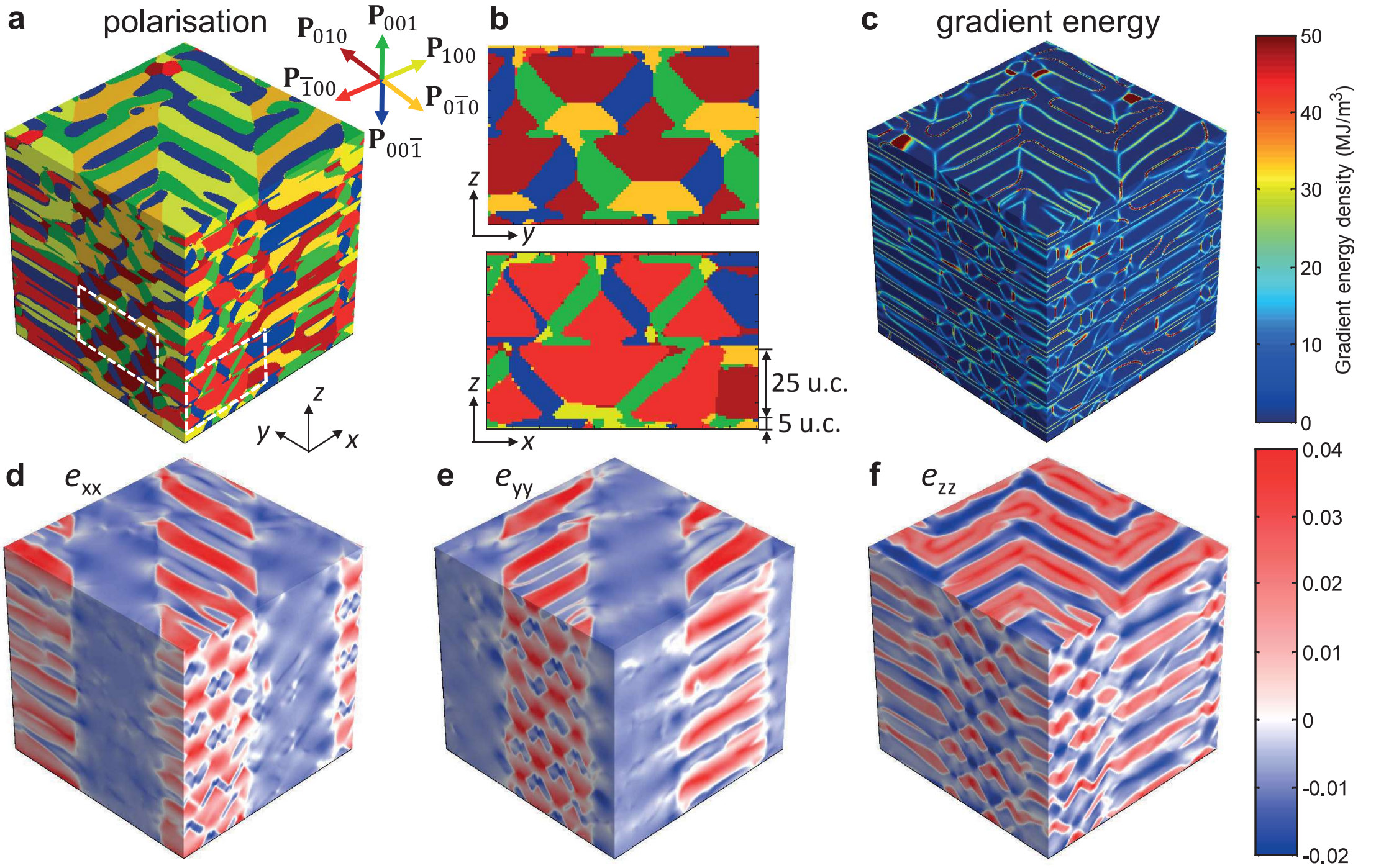
a
polarisation
$\mathbf{P}_{010}$
$\mathbf{P}_{001}$
$\mathbf{P}_{100}$
$\mathbf{P}_{\bar{1}00}$
$\mathbf{P}_{0\bar{1}0}$
$\mathbf{P}_{00\bar{1}}$
z
y
x
b
z
y
z
x
25 u.c.
5 u.c.
c
gradient energy
50
40
30
20
10
0
Gradient energy density (MJ/m^3)
d
e_{xx}
e
e_{yy}
f
e_{zz}
0.04
0.03
0.02
0.01
0
-0.01
-0.02

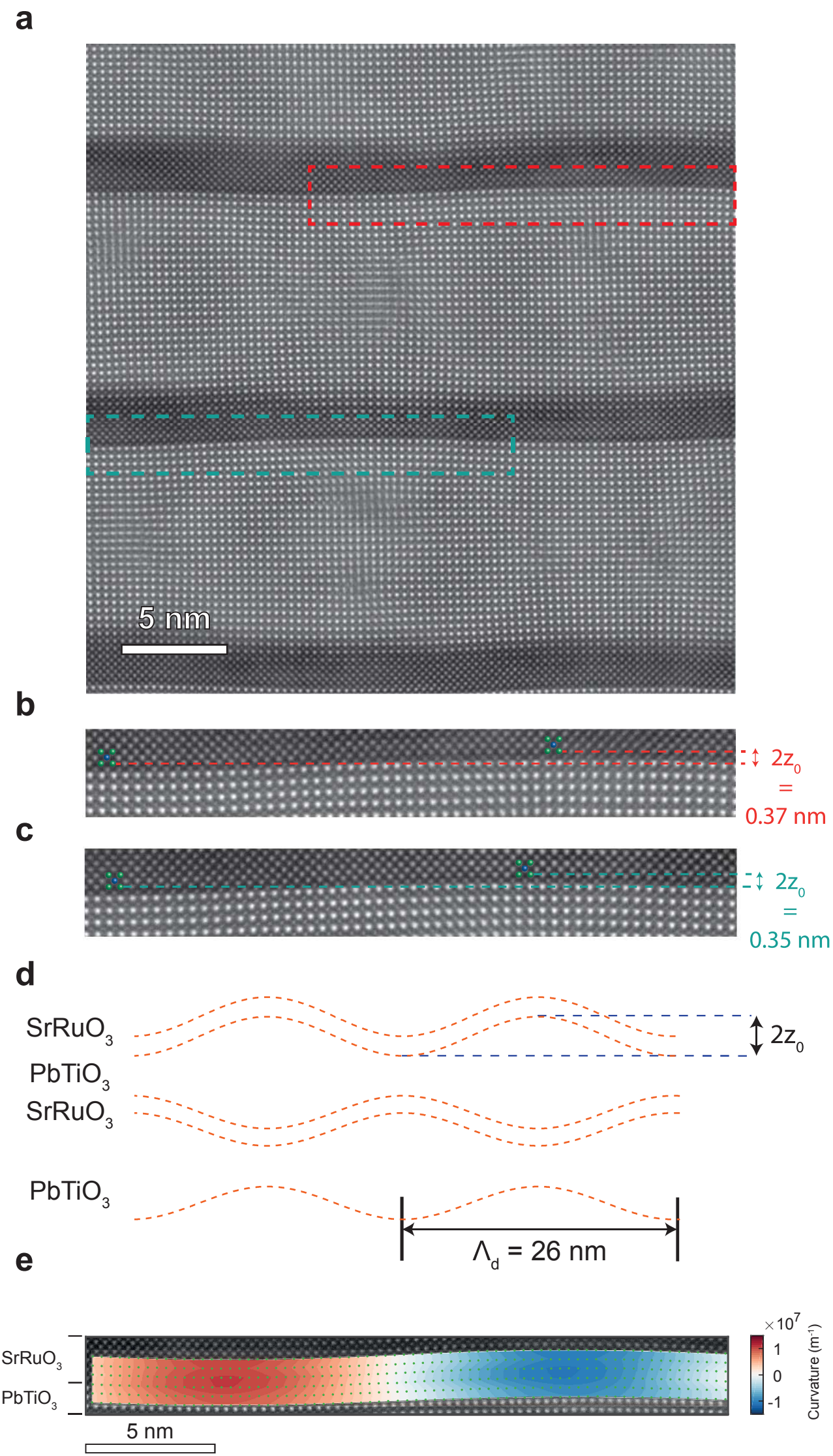
a
5 nm
b
$2z_0$ = 0.37 nm
c
$2z_0$ = 0.35 nm
d
$SrRuO_3$
$PbTiO_3$
$SrRuO_3$
$PbTiO_3$
$2z_0$
Λ_d = 26 nm
e
$SrRuO_3$
$PbTiO_3$
5 nm
$\times 10^7$
1
0
-1
Curvature (m^{-1})

Metal-ferroelectric supercrystals with periodically curved metallic layers

Marios Hadjimichael[1,2*†], Yaqi Li[2*], Edoardo Zatterin[2,3], Gilbert A. Chahine[3,4], Michele Conroy[5], Kalani Moore[5], Eoghan N. O'Connell[5], Petr Ondrejkovič[6], Pavel Marton[6], Jiri Hlinka[6], Ursel Bangert[5], Steven Leake[3], Pavlo Zubko[1,2‡]

[1]*London Centre for Nanotechnology, 17–19 Gordon Street, London WC1H 0HA, UK.*
[2]*Department of Physics and Astronomy, University College London, Gower Street, London WC1E 6BT, UK*
[3]*ESRF, The European Synchrotron, 71 Avenue des Martyrs, Grenoble 38000, France.*
[4]*Université Grenoble Alpes, CNRS, Grenoble INP, SIMAP, 38000 Grenoble, France*
[5]*Department of Physics, Bernal Institute, University of Limerick, Ireland*
[6]*Institute of Physics of the Czech Academy of Sciences, Na Slovance 2, 18221 Praha 8, Czech Republic*

Supplementary Information

Table of contents

* These authors contributed equally
† email: marios.hadjimichael@unige.ch
‡ email: p.zubko@ucl.ac.uk

Resistivity measurements

Low-temperature resistivity measurements were performed in a Janis CCS-150 closed-cycle helium cryostat between 8 K and 300 K. A 1 µA current was supplied using a Keithley 2636B SourceMeter while a Keithley 2000 Multimeter was used to measure the voltage in four-point geometry with the four corners of the sample contacted using silver paste. Resistivity values were calculated using the van der Pauw formula with the resistance values for the two orthogonal configurations obtained during separate cooling and heating runs. The reproducibility of the measurements was confirmed by repeating them multiple times. The resistivity-temperature curves obtained on heating and cooling for a PTO_{19}/SRO_5 superlattice are shown in Fig. S1.

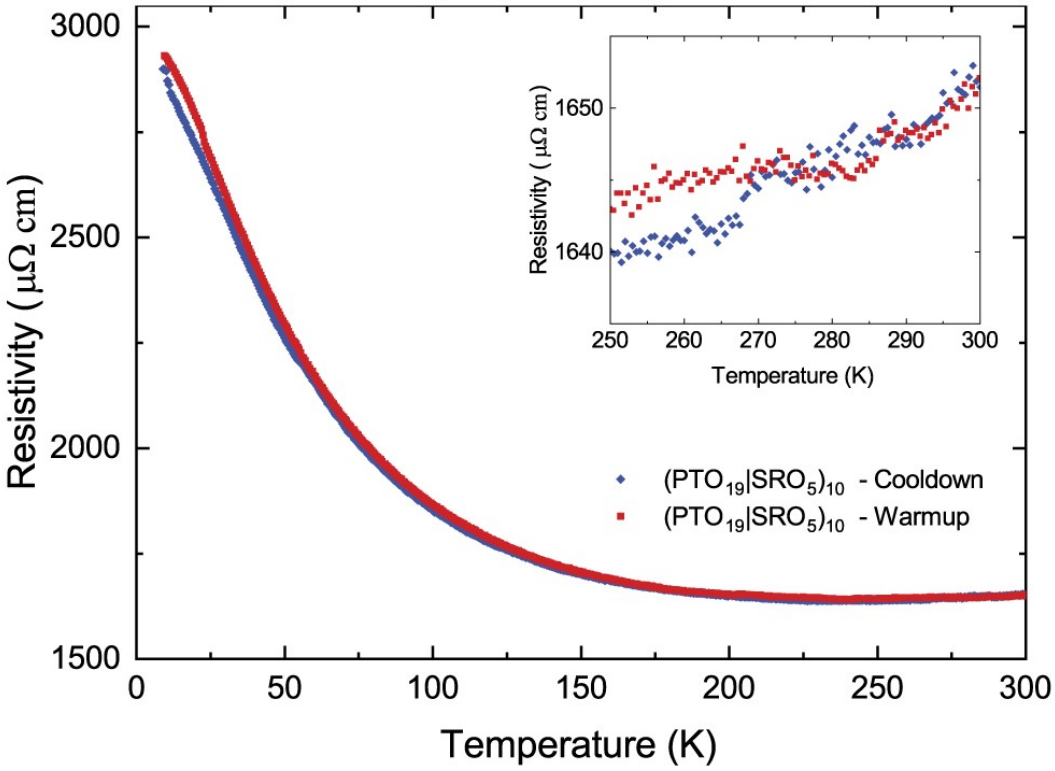

Figure S1| Resistivity-temperature curves for a PTO_{19}/SRO_5 superlattice measured on heating and cooling. The inset is a plot of the resistivity close to room temperature, showing that it exhibits metallic behaviour (resistivity increasing with temperature).

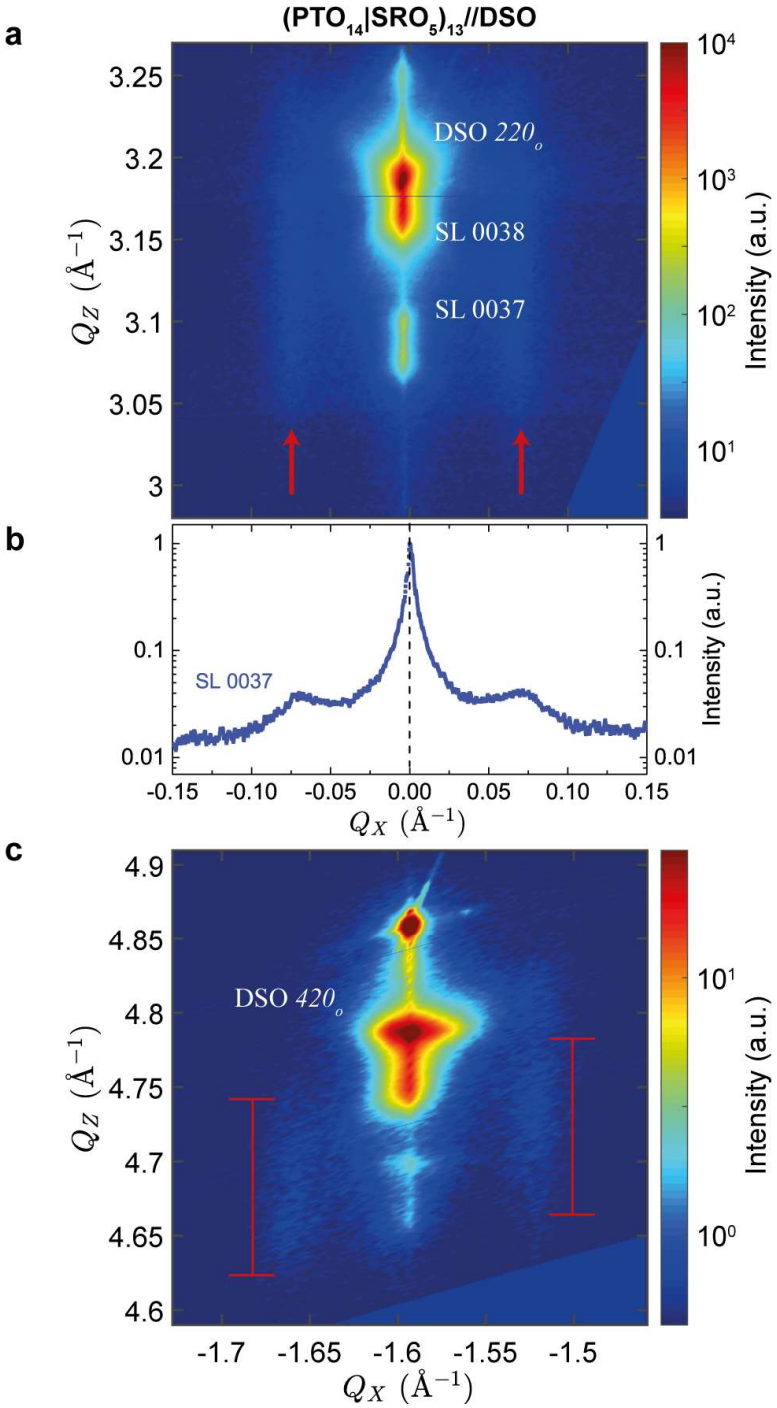

Figure S2| Reciprocal space mapping of a PTO_{14}/SRO_5 superlattice. a. Reciprocal space map around the 220_o (002_{pc}) reflection of the $DyScO_3$ substrate, showing superlattice peaks and diffuse satellite streaks indicated by red arrows. b. Intensity profile across the superlattice (SL) Bragg peak and domain satellites. c. Reciprocal space map around an off-specular 420_o (103_{pc}) reflection of the $DyScO_3$ substrate.

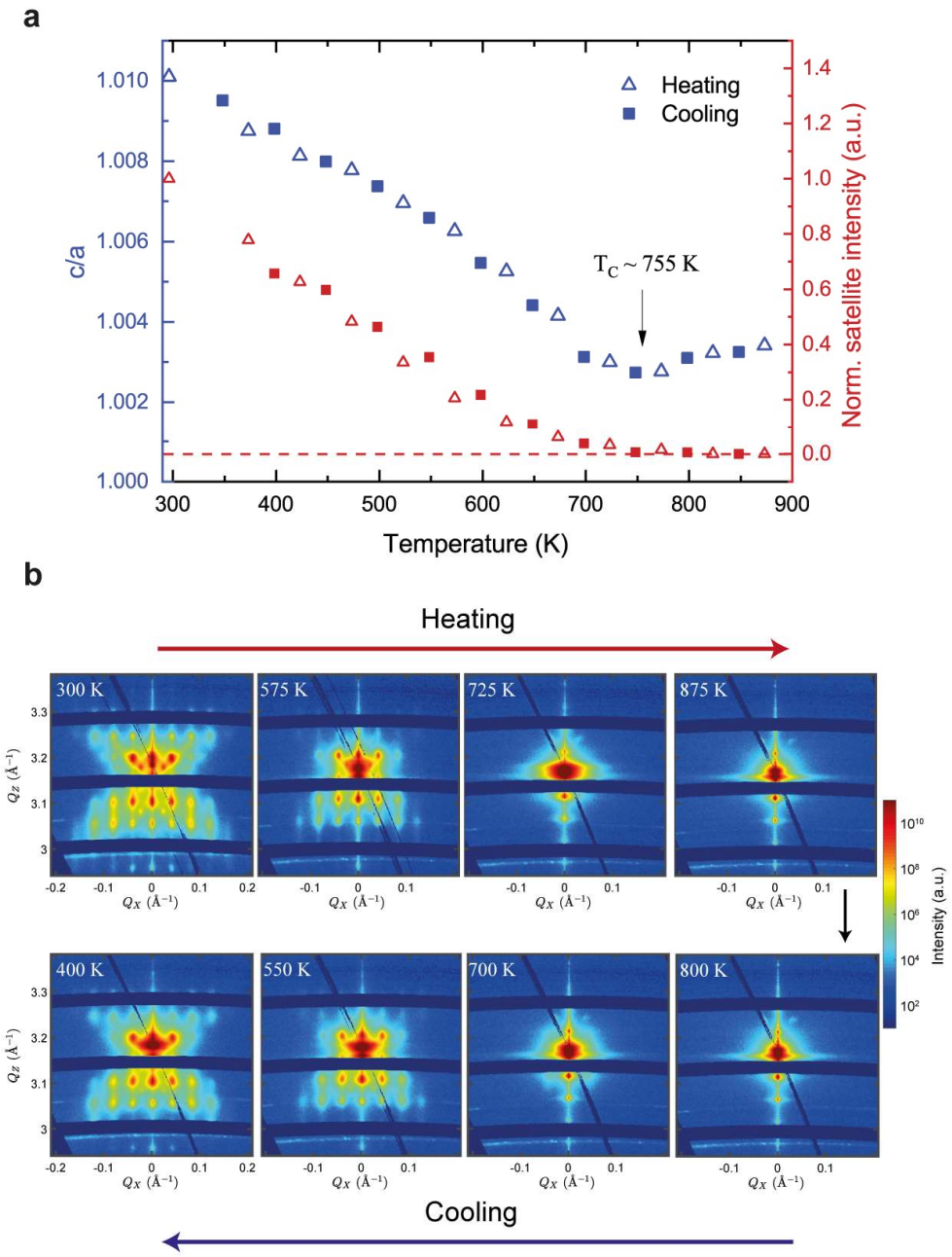

Figure S3| Temperature dependence of the supercrystal reflections for a PTO_{26}/SRO_7 superlattice. a. Temperature dependence of the average superlattice tetragonality and the satellite peak intensity around the 002_{pc} reflection of the substrate. b. Reciprocal space maps at different temperatures showing the disappearance of supercrystal reflections above T_C and their reappearance after subsequent cooling of the sample.

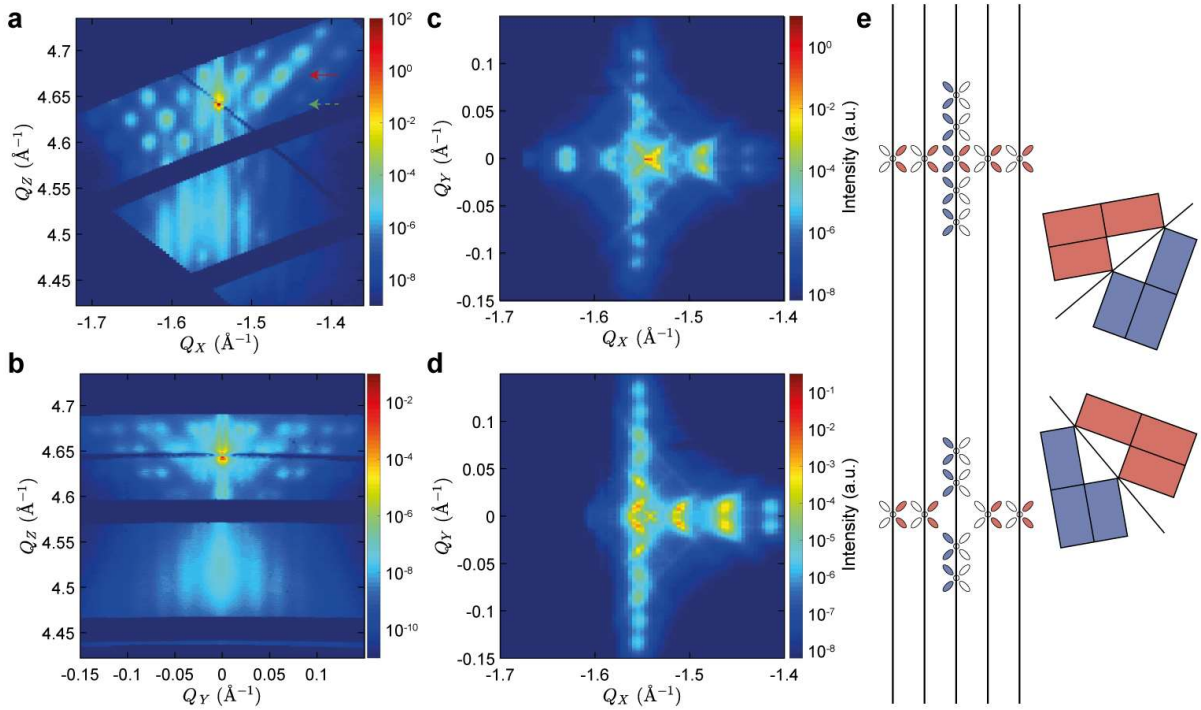

Figure S4| 2D cuts through reciprocal space of a PTO_{27}/SRO_5 superlattice around the $\bar{1}03_{pc}$ substrate peak . Panels a and b correspond to the planes $Q_Y = 0$ and $Q_X = 0$ respectively. Panels c and d correspond to the planes at Q_z=4.649 Å^{-1} and Q_z=4.672 Å^{-1} , as marked by the dashed green and solid red arrows in panel a respectively. A clear splitting of the satellite peaks due to in-plane twinning is observed. e. Schematics highlighting the domain variants responsible for each reflection in c and d.

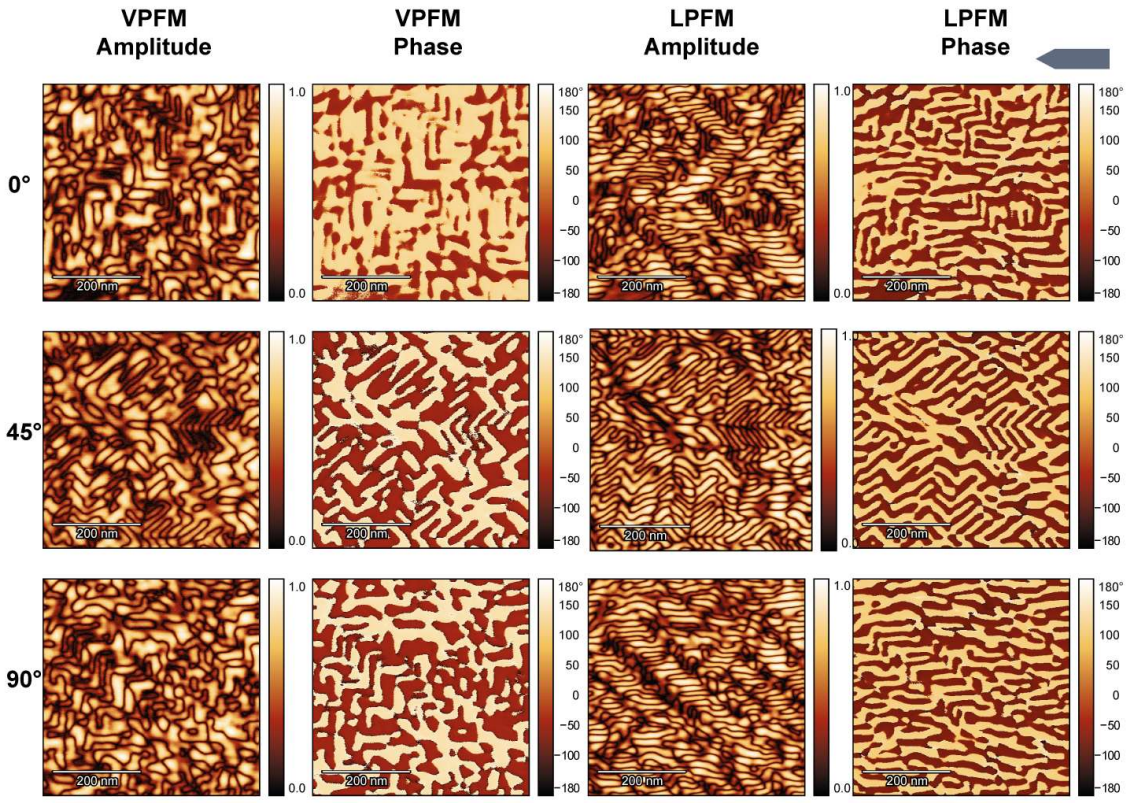

Figure S5|Vertical and lateral PFM amplitude (normalised) and phase images of the 3D domain structure measured for different cantilever orientations with respect to the sample.

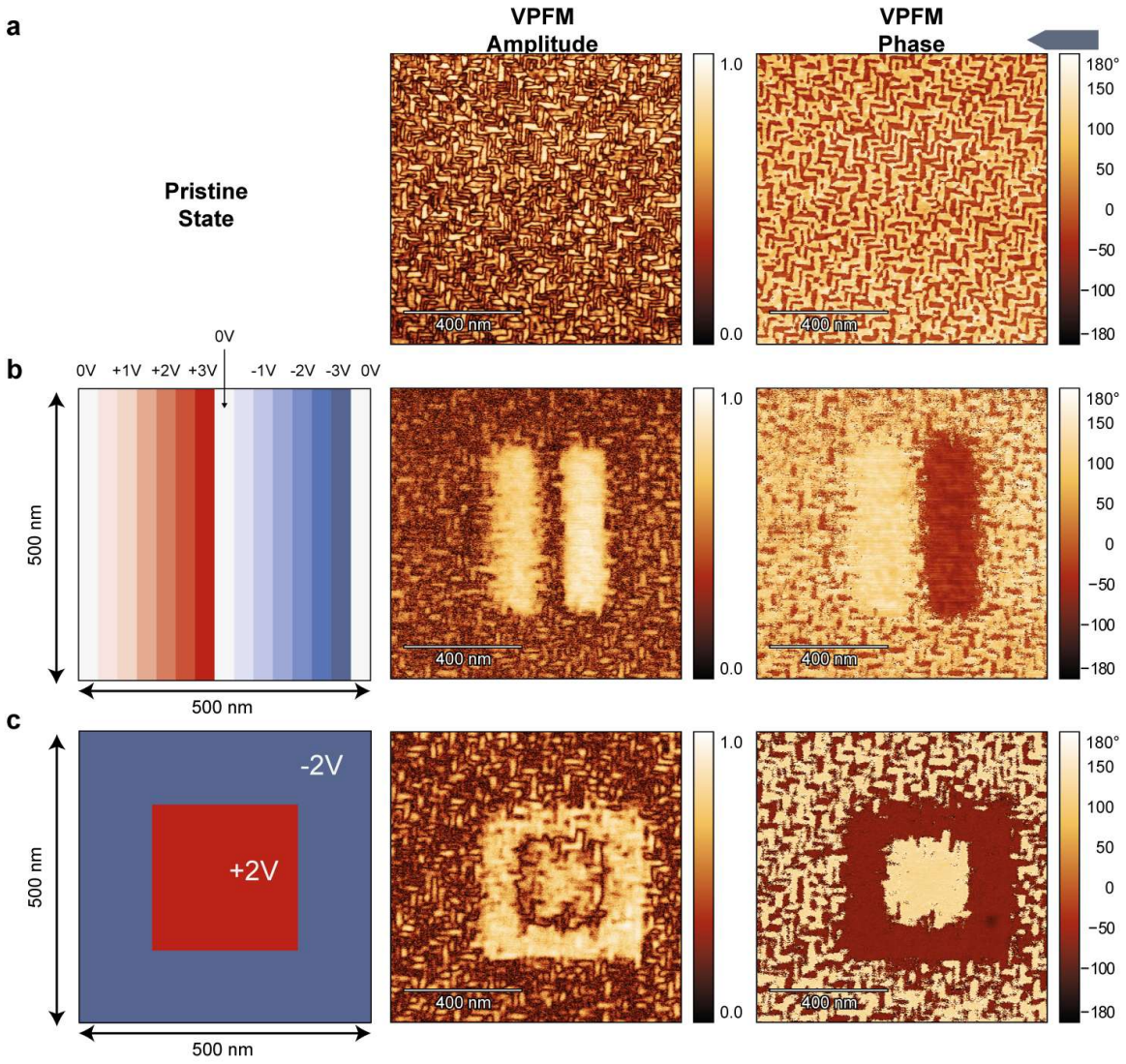

Figure S6| PFM switching studies. VPFM amplitude (normalised) and phase images for (a) the pristine (unpoled) state, and after poling the sample using positive and negative bias applied to the sample in two different ways: (b) by ramping up the voltage from 0 V to +3 V and then from 0 V to −3 V, and (c) by writing a 500 nm × 500 nm square with −2 V, followed by a 250 nm × 250 nm square with +2 V inside it. In both cases, application of a DC bias while scanning the tip produces regions with uniform VPFM phase. At the same time, VPFM amplitude images retain signatures of domain walls, indicating that while the out-of-plane polarisation is dominated by one variant, the underlying periodic domain structure has not fully switched. We have found that the poled states slowly revert back to the original unpoled structure, with different timescales for different polarisation directions; regions poled with positive bias applied to the sample return to the original structure faster than ones poled with negative bias, presumably due to the different boundary conditions at the surface and bottom interface of the top $PbTiO_3$ layer.

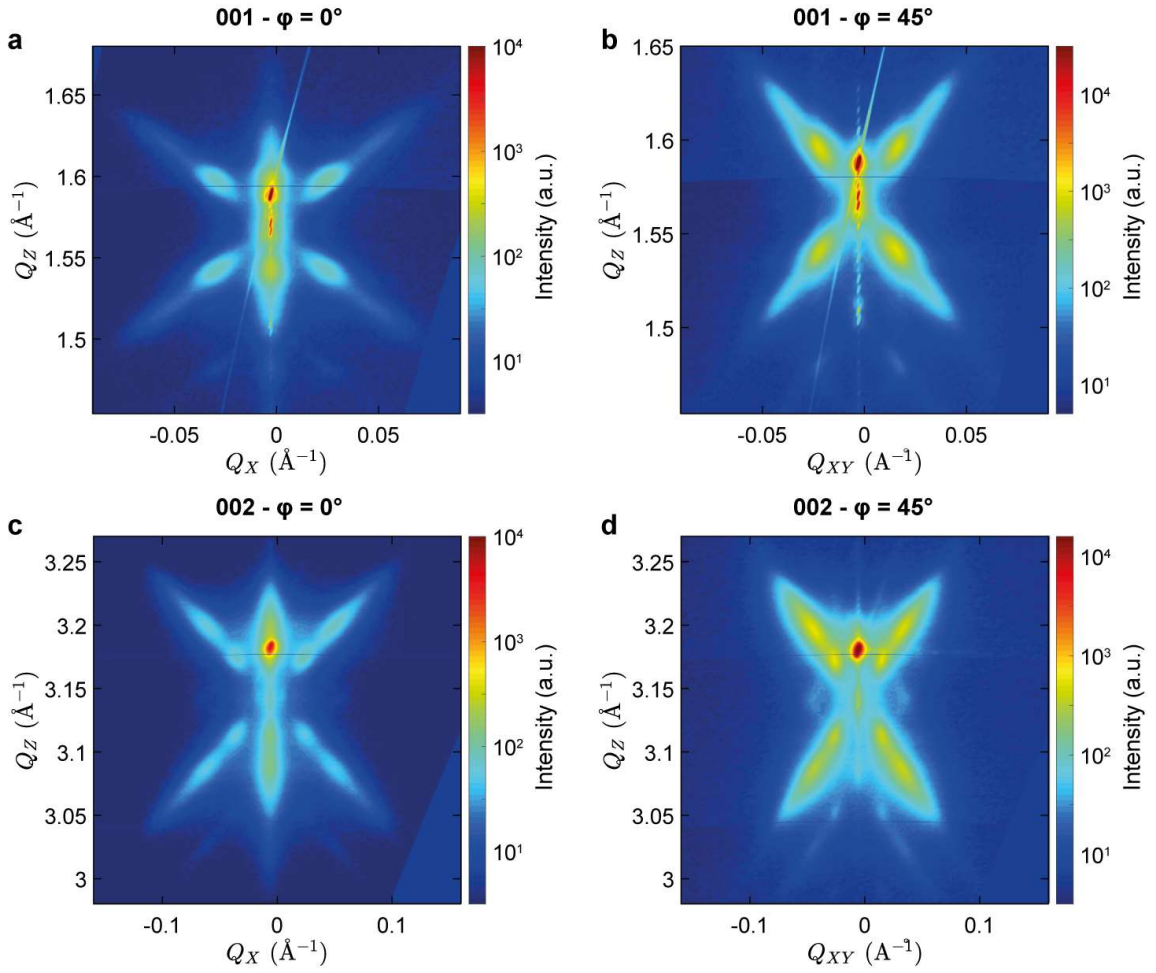

Figure S7| Reciprocal space maps around the 001_{pc} and 002_{pc} reflections of the $DyScO_3$ substrate obtained using a laboratory diffractometer for the hierarchical superlattice described in Fig 4 of the main text. Due to the divergence of the beam perpendicular to the scattering plane, intensity from the supercrystal reflections outside of the scattering plane is projected onto it, leading to the appearance of additional spurious 'superlattice' peaks on the CTR when the scattering plane is parallel to $<100>_{pc}$ (panels a and for $\phi = 0°$). These can be avoided by rotating the sample by 45° around its azimuth so that the scattering plane is parallel to $<110>_{pc}$, as shown in panels b and d ($\phi = 45°$).

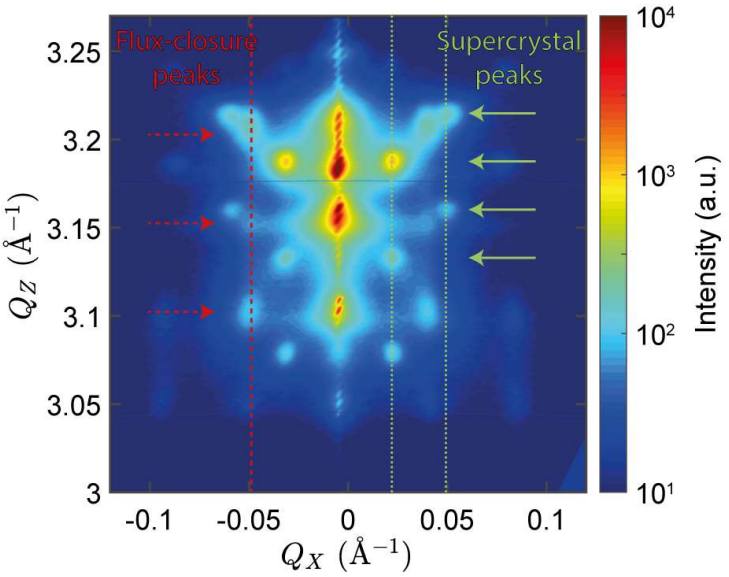

Figure S8| Reciprocal space map around the 220_o (002_{pc}) reflection of the $DyScO_3$ substrate for a PTO_{23}/SRO_7 superlattice (obtained using a laboratory diffractometer), showing superlattice peaks and domain satellite peaks which correspond to two different types of domain structures: horizontal arrows and vertical lines indicate the Q_z and Q_x positions of the supercrystal satellite peaks (in green) and the vortex satellite peaks (in red).

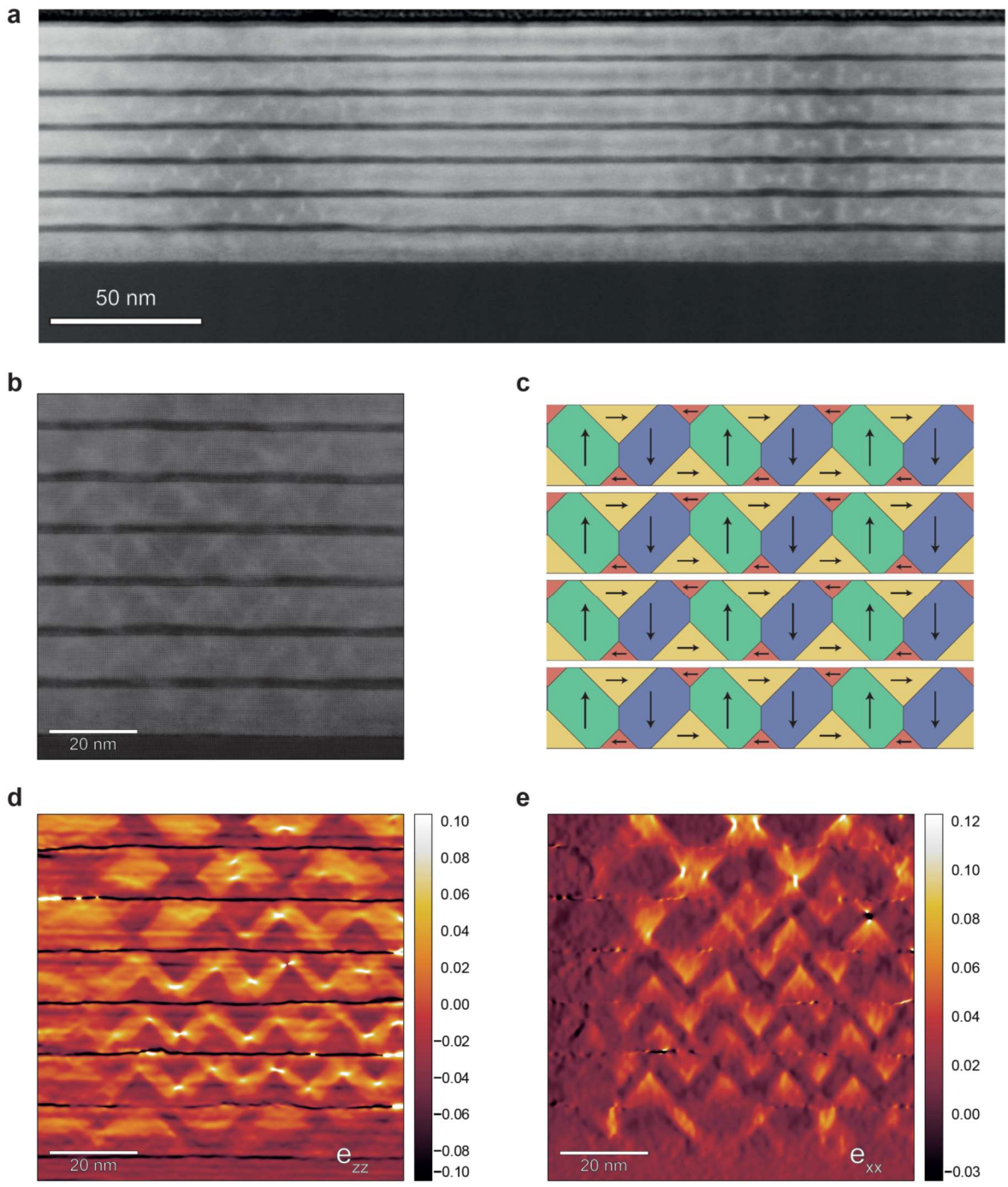

Figure S9| TEM images of flux-closure phase. a. Large scale TEM image showing the flux-closure (left) and supercrystal (right) phases side by side. b. TEM image of the flux-closure phase with a schematic of the polarisation arrangement shown in c. GPA analysis of the out-of-plane (d) and in-plane (e) strain with respect to the $DyScO_3$ substrate.

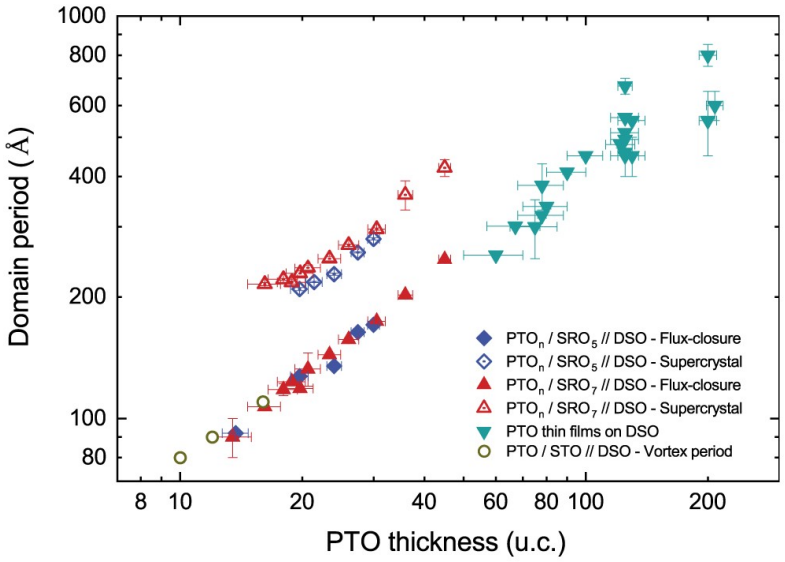

Figure S10| Domain period for the various samples measured in this study as a function of $PbTiO_3$ layer thickness. Blue diamonds and red triangles are the periods for $PbTiO_3/SrRuO_3$ superlattices on $DyScO_3$ substrates with $SrRuO_3$ thickness equal to 5 and 7 unit cells respectively. Solid and empty markers correspond to the periods of the conventional flux-closure phase and the supercrystal phase respectively. Light blue inverted triangles show the domain periods of flux-closure domains in $PbTiO_3$ thin films on $DyScO_3$, also measured in this study. Empty circles indicate the domain periods of vortices in $PbTiO_3/SrTiO_3$ superlattices on $DyScO_3$ substrates, extracted from References [1-3]. The plot shows a nearly perfect matching of the vortex periods in $PbTiO_3/SrTiO_3$ superlattices with the periods of the flux-closure phase in $PbTiO_3/SrRuO_3$ superlattices.

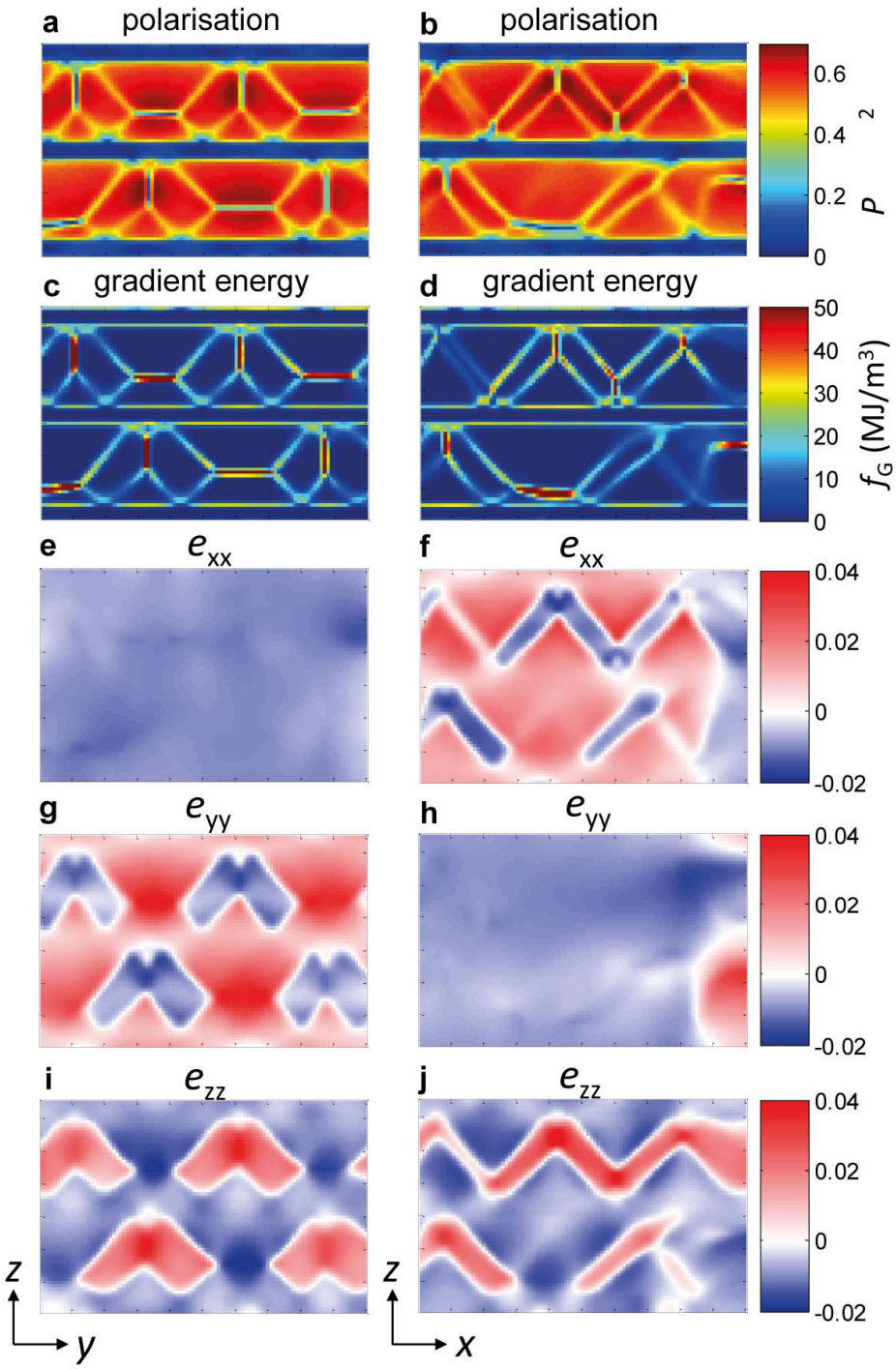

Figure S11| Detailed view on the competing domain patterns obtained in phase-field simulations described in Fig. 5 of the main text. The areas are the same 100x65 sites (40x26 nm^2) as those indicated by the rectangles in Fig. 5a and Fig. 5b. Left panels show vertical and horizontal flux closure patterns (as in the top of Fig. 5b), right panels show the competing zigzag pattern (bottom of Fig. 5b). a. and b. Magnitude of polarisation, c. and d. density of gradient energy, e.-j. components of inhomogeneous strain.

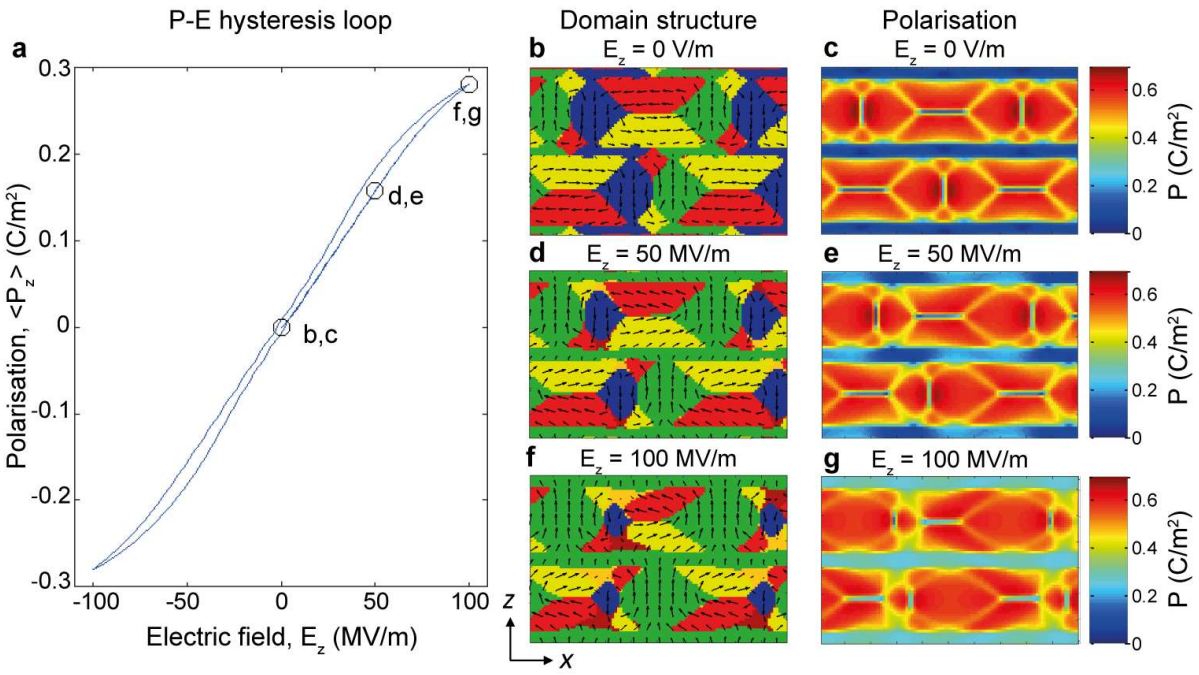

Figure S12| Phase-field simulations of the supercrystal response to an out-of-plane electric field. **a**. Polarisation-electric field (*P-E*) hysteresis loop from a relaxed structure with flux-closure patterns. **b-g**. Domain structure and polarisation under electric field strengths indicated by empty circles in the loop. Domain patterns show that the field-induced polarisation results from domain wall displacements within each domain period. Domains with out-of-plane polarisation aligned parallel to the field grow at the expense of those aligned antiparallel to the field and the in-plane flux-closure components.

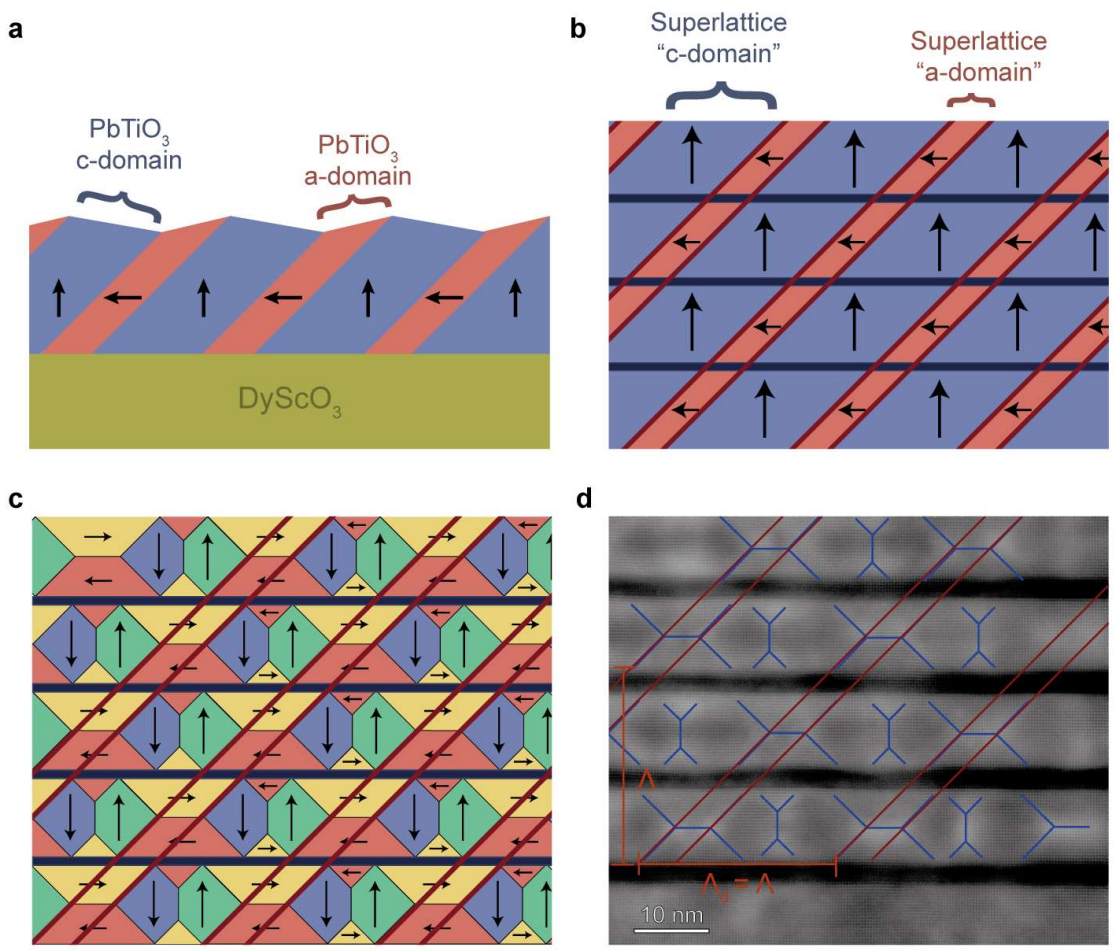

Figure S13| Schematic explaining the origin of the supercrystal phase. a. Schematic of an *a/c* domain configuration in a $PbTiO_3$ thin film deposited on a $DyScO_3$ substrate. The *a* and *c* domains are separated by $(101)_{pc}$ domain walls. b. The same *a/c* domain configuration superimposed on a $PbTiO_3/SrRuO_3$ superlattice, assuming perfect screening (monodomain $PbTiO_3$). c. Supercrystal structure formed due to imperfect screening of the $PbTiO_3$ polarisation at the metal-ferroelectric interfaces, where the depolarising field forces non-polar flux-closure polarisation configurations. d. STEM HAADF image of the $PbTiO_3/SrRuO_3$ superlattice in the main text, with domain walls sketched in blue.

Calculation of the curvature in the $SrRuO_3$ layers

The positions of Ti and Ru atoms in the $PbTiO_3$ and $SrRuO_3$ layers respectively were extracted using the Atomap package [4]. The position of each atomic plane was fitted with the following sinusoidal function:

$$z = z_0 \sin\left(\frac{2\pi(x+b)}{L}\right) + c$$

where z_0, b, L and c are adjustable parameters. The local curvature $\kappa = z''/\left(1+z'^2\right)^{3/2} \approx z''$ was calculated analytically for each plane by taking the second derivative $z'' = \partial^2 z/\partial x^2$ of the above equation with the parameters obtained from the fit to the data, as shown in Fig. S15 and Table S1. The contribution from the first derivative $z' = \partial z/\partial x$ was found to be negligible (maximum $z'^2 \approx 0.002$).

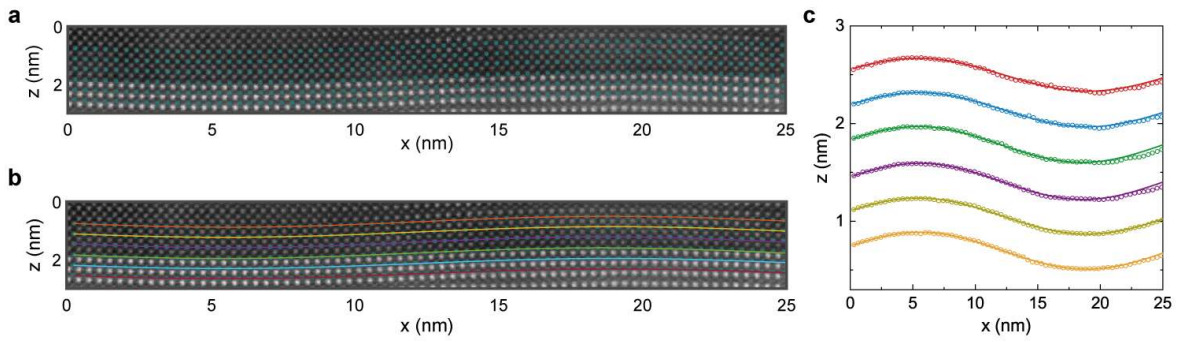

Figure S14| Curvature estimation. a. HAADF image with atomic positions of B cation centres located using Atomap software indicated as blue dots. b and c. Sinusoidal fits (solid lines) for the atomic positions (circles) in each row from which the curvature is obtained.

Plane	z_0 (nm)	z_0 error (nm)	b (nm)	b error (nm)	L (nm)	L error (nm)	c (nm)	c error (nm)	max. curvature (m^{-1})
1	0.189	0.002	1	1	26.6	0.3	0.699	0.002	1.05E+07
2	0.184	0.002	1.3	0.9	27.0	0.4	1.053	0.002	9.96E+06
3	0.185	0.002	1.0	0.4	26.2	0.3	1.409	0.002	1.06E+07
4	0.184	0.002	1.1	0.4	26.2	0.3	1.787	0.002	1.05E+07
5	0.175	0.002	1.3	0.6	27.0	0.5	2.142	0.003	9.45E+06
6	0.168	0.003	1.4	0.9	27.3	0.7	2.501	0.004	8.90E+06

Table S1| Parameters obtained from fitting the atomic displacements to a sinusoidal function.

Supplementary video|Synchrotron X-ray diffraction 3D reciprocal space map around the 002_{pc} reflection of the DyScO3 substrate for a PTO_{31}/SRO_7 PbTiO3/$SrRuO_3$ superlattice.

References

1 Damodaran, A. R. *et al.* Phase coexistence and electric-field control of toroidal order in oxide superlattices. *Nat Mater* **16**, 1003-+, doi:10.1038/Nmat4951 (2017).

2 Shafer, P. *et al.* Emergent chirality in the electric polarization texture of titanate superlattices. *P Natl Acad Sci USA* **115**, 915-920, doi:10.1073/pnas.1711652115 (2018).

3 Yadav, A. K. *et al.* Observation of polar vortices in oxide superlattices (vol 530, pg 198, 2016). *Nature* **534**, 138-138, doi:10.1038/nature17420 (2016).

4 Nord, M., Vullum, P. E., MacLaren, I., Tybell, T. & Holmestad, R. Atomap: a new software tool for the automated analysis of atomic resolution images using two-dimensional Gaussian fitting. *Adv Struct Chem Imag* **3**, doi:10.1186/s40679-017-0042-5 (2017).